



## RESEARCH INTERNSHIP REPORT

MECHANICS - MODELLING IN MECHANICS

2019-2020

---

# Detonation Initiation by Shock Wave Refraction

---

*Author (Promotion):*

Mathilde DUTREUILH (2021)

*ENSTA supervisor:*

Pr. Karsten PLAMANN  
Professeur ENSTA Paris

*External advisor:*

Dr. Rémy MÉVEL  
Professeur Associé  
Tsinghua University  
School of Vehicle and Mobility

*Host organism:*

Institut P'

CNRS - Université de Poitiers  
ISAE-ENSMA - UPR 3346  
11 Boulevard Marie et Pierre Curie  
Site du futuroscope  
86073 POITIERS CEDEX 9

*Host organism advisor:*

Dr. Josué MELGUIZO-GAVILANES  
CNRS Chargé de recherche

**Non confidential and publishable report on the Internet**

Internship completed from May 18 to July 31, 2020.



## **NON CONFIDENTIALITY NOTICE**

The present document is not classified as confidential. It is thus available online for consultation by all.

## ACKNOWLEDGMENTS

*I would like to express my great appreciation to Dr. Mével and Dr. Melguizo-Gavilanes for their availability, their patience and the many suggestions they gave me during the research project.*

*I would also like to offer my special thanks to Pr. Plamann for answering my questions and for providing helpful advice whenever I needed it.*

*Thank you to Stany Gallier from ArianeGroup for providing finite element results.*

*I am particularly grateful for the assistance given by Yann de Gouvello, former intern on this subject, who gave me the opportunity to continue his work.*

*Thank you to my parents who hosted me for three months.*

## ABSTRACT

The present document summarizes the studies made on shock wave refraction at a slow-fast gas-gas interface. It revisits basic shock wave concepts and analysis tools both by exploring reference articles and extending the work of a former intern on the topic. Both regular and irregular refraction structures are described, along with their transition boundaries. After some critical considerations on the assumptions made to compute these boundaries, the method is applied to a reactive interface using a set of MATLAB scripts. Further results are presented in which reactive computations are conducted following the thermodynamic changes that a fluid particle experiences as it travels through a regular refraction pattern. Conditions for detonation initiation on Mach number of the incident flow are found for regular refraction patterns.

## KEYWORDS

Gas dynamics, shock wave refraction, super-knock, combustion, Lagrangian particles.



# List of Figures

1.1 Comparison of light and shock wave refraction . . . . .	6
1.2 Polar diagram for RRE structure . . . . .	8
1.3 Illustration of RRE structure . . . . .	9
1.4 Polar diagram for RRR structure . . . . .	10
1.5 Illustration of RRR structure . . . . .	11
1.6 Polar diagram for BPR structure . . . . .	12
1.7 Illustration of BPR structure . . . . .	13
1.8 Illustration of FPR structure . . . . .	14
1.9 Illustration of FNR structure . . . . .	15
1.10 Illustration of TNR structure . . . . .	15
1.11 Illustration of LSR structure . . . . .	16
1.12 Comparative regime diagram for the CO <sub>2</sub> -CH <sub>4</sub> interface . . . . .	18
1.13 Schematic for the piston theory . . . . .	19
1.14 Optimization of the ratio of piston velocities . . . . .	20
1.15 Comparative regime diagram for the CO <sub>2</sub> -CH <sub>4</sub> interface with correction for FPR-TNR transition . . . . .	22
1.16 Comparative regime diagram for the Air-CH <sub>4</sub> interface . . . . .	24
2.1 Regime diagram for the H <sub>2</sub> -O <sub>2</sub> -He interface. . . . .	28
2.2 Notations, zones and angles for RRE pattern . . . . .	30
2.3 RRE - Schematic of the path of several particles . . . . .	31
2.4 RRE - Evolution of state variables for several particles . . . . .	31
2.5 RRE - Evolution of state variables for a given particle . . . . .	32
2.6 RRE - Chemical simulation for a given particle . . . . .	32
2.7 RRE - Chemical simulation for several particles . . . . .	33
2.8 RRE - Evolution of $M_{\text{ignit}}$ . . . . .	34
2.9 Notations, zones and angles for RRR pattern . . . . .	34
2.10 RRR - Schematic of the path of several particles . . . . .	35

2.11 RRR - Evolution of state variables for several particles . . . . .	35
2.12 RRR - Evolution of state variables for a given particle . . . . .	36
2.13 RRR - Chemical simulation for a given particle . . . . .	37
2.14 RRR - Evolution of the reflected pressure jump $\xi_r$ with the free-stream Mach number $M_1$ . . . . .	37
2.15 RRR - Chemical simulation for several particles . . . . .	38
2.16 Regime diagram for $H_2\cdot O_2\cdot He$ interface . . . . .	39
2.17 Simulation of a BPR structure for a Ar-He interface . . . . .	39
2.18 Notations, zones and angles for BPR pattern . . . . .	40
A.1 Change of frame of reference . . . . .	45
A.2 Geometry associated to the oblique shock . . . . .	46
B.1 RRE to RRR transition . . . . .	50
B.2 RRR to BPR transition . . . . .	50
B.3 FPR to TNR . . . . .	51
C.1 Schedule of the internship . . . . .	54

# Contents

<b>Acknowledgments</b>	<b>ii</b>
<b>Abstract</b>	<b>iii</b>
<b>List of figures</b>	<b>vi</b>
<b>Introduction</b>	<b>1</b>
<b>1 Shock Wave Refraction over an interface: a Gas Dynamics problem</b>	<b>5</b>
1.1 Generalities on refraction structures . . . . .	5
Definitions and concepts . . . . .	5
Regular refraction patterns . . . . .	8
Irregular refraction patterns . . . . .	10
1.2 Map of the refraction domains for the CO <sub>2</sub> -CH <sub>4</sub> interface . . . . .	17
Discrepancies analysis and possible improvements . . . . .	19
Piston theory . . . . .	19
Membrane inertia . . . . .	20
1.3 Map of the refraction domains for the Air-CH <sub>4</sub> interface . . . . .	23
<b>2 Reactive interface: detonation initiation by refraction</b>	<b>27</b>
2.1 Map of the refraction domain for the H <sub>2</sub> -O <sub>2</sub> -He interface . . . . .	27
2.2 Path of a Lagrangian particle: general method . . . . .	29
2.3 Detonation initiation for regular patterns . . . . .	29
Regular Refraction with reflected Expansion . . . . .	29
Evolution inside the expansion wave . . . . .	29
Gas dynamics results . . . . .	30
Reactive results . . . . .	31
Regular Refraction with Reflected shock . . . . .	33
Gas dynamics results . . . . .	34
Reactive results . . . . .	36

Non-monotonic evolution of the reflected pressure jump . . . . .	36
2.4 Failure of the general method for irregular pattern . . . . .	38
<b>Conclusions</b>	<b>41</b>
<b>Bibliography</b>	<b>41</b>
<b>Appendices</b>	<b>44</b>
<b>A Shock wave and Prandtl-Meyer relationship in gas dynamics</b>	<b>45</b>
A.1 Change of frame of reference . . . . .	45
A.2 Shock-jump equations . . . . .	46
A.3 Prandtl-Meyer equations . . . . .	47
<b>B Transition criteria in the regime diagram (<math>\chi - \omega</math>)</b>	<b>49</b>
B.1 RRE to RRR or BPR boundary . . . . .	49
B.2 RRR to BPR boundary . . . . .	49
B.3 BPR to FNR boundary . . . . .	51
B.4 FPR to TNR boundary . . . . .	51
B.5 TNR to LSR boundary . . . . .	52
<b>C Schedule of the internship</b>	<b>53</b>

# Introduction

## HOST ORGANISM AND SPECIFICITY OF THE INTERNSHIP

The present internship report follows up on [de Gouvello's](#) report, written in 2019. A large part of his work have been revisited, corrected and improved in the present internship: a short collaboration has made it possible to save an important amount of time.

Due to the COVID-19 crisis, the internship was adapted to offer the best working conditions given the sanitary constraints. It was initially planned to take place at the School of Vehicle and Mobility at Tsinghua University, Beijing, China, under Dr. Rémy Mével's supervision. Unfortunately, the current context required French students to stay in their home country. Dr. Josué Melguizo-Gavilanes, from *'l'Institut P'* in Poitiers, offered to supervise the internship with the originally proposed topic. Dr. Mével and Dr. Melguizo-Gavilanes have thus advised me for eleven weeks.

## THE SUPER-KNOCK PHENOMENON

Combustion is still a leading source of energy in the automotive industry and internal combustion engines are required to reduce their greenhouse gases emissions to fit the ever increasing regulations [[de Gouvello, 2019](#)]. When it comes to spark-ignition internal combustion engine (SI-ICE), present in gasoline cars, one of the most promising strategies is to increase their power density by increasing boost and downsizing engines [[Wang et al., 2017a](#), [Qi et al., 2015](#), [Wang et al., 2017b](#)]. Practically, this is achieved by increasing the engine's compression ratio [[Netzer et al., 2018](#)]. However, under such conditions, super-knock can occur: it corresponds to the initiation of a detonation within the engine cylinder. Super-knock events are characterized by extremely high pressure peaks and by large-amplitude high-frequency pressure oscillations , i.e. several MPa. Due to these extreme pressure peaks and oscillation amplitudes, a single event can result in irreversible damage to the engine [[Wang et al., 2017a](#)]. Consequently, super-knock constitutes a major obstacle for the development of next generation SI-ICE.

Super-knock is observed in the low-speed, high-load regime and is characterized by three phases: (i) pre-ignition; (ii) auto-ignition in the end-gas; and (iii) detonation initiation and propagation. Pre-ignition is a random event and is related to the formation of a hot spot from a lubricating oil droplet or from a carbon deposit [Wang et al., 2017b]. Due to the end-gas' high temperature and pressure, a local explosion in the highly compressed unreacted mixture is observed and the rapid expansion of the gas induces the formation of a shock wave [Wang et al., 2017b, 2015, 2016, 2018]. During the third phase, the shock wave initiated by the end-gas local explosion can interact with the engine's cylinder walls, the pre-ignition flame, or additional shock waves created at different locations within the end-gas, and lead to detonation onset, i.e., a super-knock event [Wang et al., 2017b, 2015, 2016, 2018].

Experiments performed in a rapid compression machine (RCM, see de Gouvello [2019]) enabled the identification of three “modes” of super-knock initiation based on the dynamics of the shock wave generated by the local explosion in the end-gas: (i) Shock Wave Reflection Induced Detonation (SWRID); (ii) Shock Wave and Flame front Induced Detonation (SWFID); (iii) Shock Wave Focusing Induced Detonation (SWFoID). The mode of super-knock initiation was found to depend on the energy density of the reactive mixture [Qi et al., 2015, Wang et al., 2016, 2018].

The present report focuses on the second mode of super-knock initiation. Wang et al. showed, by combining high-speed experimental imaging and numerical simulation, that the interaction between the shock wave generated by the end-gas auto-ignition and the spherical flame creates a region of high pressure and temperature that enables flame front acceleration and detonation onset. However, the high computational cost of the reactive simulation performed by Wang et al. prevented the use of a mesh size adequate to resolve the detailed structure of the refracting shock wave.

Shock wave refraction results from the interaction between a shock wave and an interface, i.e. gas-gas or gas-liquid [Nourgaliev et al., 2005]. In the context of super-knock, only the slow-fast gas-gas interfaces are relevant, characterized by the incident phase having a lower acoustic impedance (defined as the product of the gas density and the local speed of sound) than the transmitted phase [Henderson, 1970]. Depending on the angle between the shock wave and the interface, and on the incident shock Mach number, refraction can either be regular or irregular [Han and Yin, 1993]. Several structures have been observed for both regular and irregular refraction [Han and Yin, 1993].

Shock wave refraction has been extensively studied experimentally and theoretically by Henderson's group [Abd-El-Fattah et al., 1976, Abd-El-Fattah and Henderson, 1978] and a theoretical regime diagram constructed Abd-El-Fattah and Henderson [1978]. However, the exact methodology employed to establish the aforementioned diagram was not outlined in detail and it is required to study many of their papers to clearly understand the methodology used [Abd-El-Fattah et al., 1976, Abd-El-Fattah and Henderson, 1978, Henderson et al., 1991, Henderson, 1989, 1966]. While several other studies were performed on shock wave refraction

over flat, cylindrical, spherical, and elliptical gas-gas interfaces [Zeng and Takayama, 1996, Hass and Sturtevant, 1987, Zhang et al., 2019], none of them revisited Henderson's regime diagram, nor a clear connection between refraction and super-knock could be made, likely because these studies were carried out before unambiguous experimental evidence of super-knock became available [Wang et al., 2015].

The goal of the present report is to provide a detailed overview of the structures of shock wave refraction at a slow-fast gas-gas reactive interface and to determine at which critical conditions ignition could occur. First, fundamental concepts of shock wave refraction are described. Then, the work of a former intern [de Gouvello, 2019] on the possible refraction patterns is critically reviewed. Finally, reactive computations accounting for the thermodynamic changes that a fluid particle experiences as it travels through a regular refraction pattern are carried out (i.e. following a Lagrangian formulation).



# 1. Shock Wave Refraction over an interface: a Gas Dynamics problem

The present chapter gives relevant definitions and concepts before describing several regular and irregular refraction patterns for a given type of interface, i.e. the slow-fast interface. The goal is to describe the main characteristics of regular and irregular patterns and what are the main parameters that control the refraction structure.

## 1.1 GENERALITIES ON REFRACTION STRUCTURES

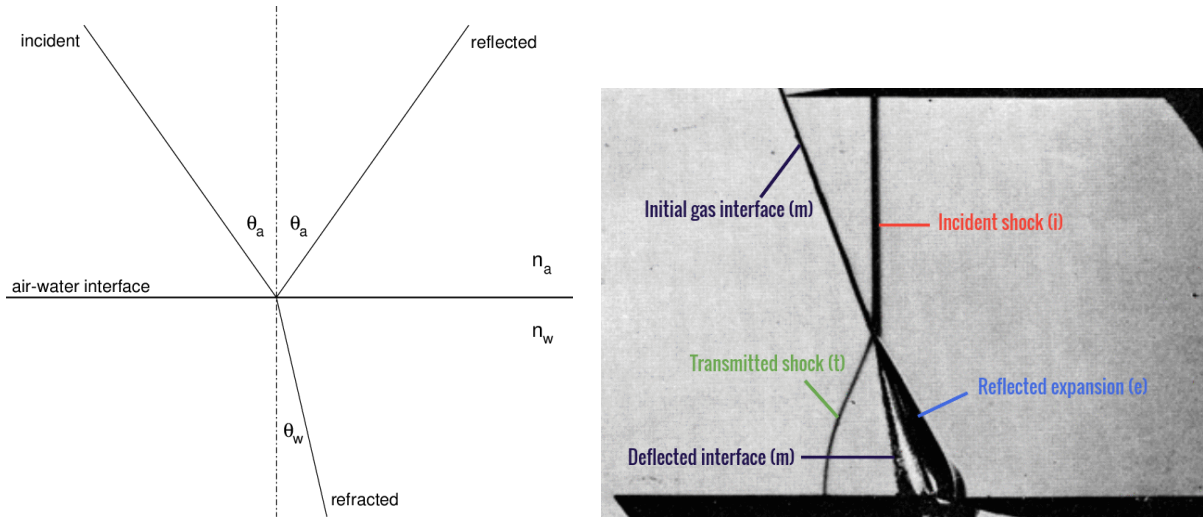
The refraction phenomenon is characterized by the deflection of a wave which encounters an interface between two media where the speed of propagation of the wave is different. In the case of light refraction, which is the more commonly known, the incident wave is divided at the interface: the transmitted wave is deflected in the second medium and the reflected wave travels back in the first medium.

Shock wave refraction is a wide and complex subject which requires basic knowledge of gas dynamics. As for light refraction, three waves are noticeable in regular shock wave refraction: incident, reflected and transmitted or refracted, as illustrated in figure 1.1 (a) and (b). However, some differences are evident while examining the (b) schematic: the interface is deflected behind the shock, the reflected wave has not the same structure as the other two waves, angles between the waves and the interface seem to obey a certain law, different from light propagation.

Under specific conditions, irregular patterns can even be observed for a shock wave refraction. The phenomenon becomes more complex to describe and the analogy with light no longer holds: shock wave propagation laws are needed.

### Definitions and concepts

- **The interface:** refraction occurs at an interface between two media where a shock wave can propagate. It is labeled by the "m" line in figure 1.1 (b). It can be a gas-liquid or a



(a) Light refraction at an air-water interface (schematic):  $n_{a,w}$  refractive index of the air/water;  $\theta_{a,w}$  angle between the light ray and the interface normal in the air/water.

(b) Regular shock wave refraction at a  $\text{CO}_2\text{-CH}_4$  interface (schlieren photograph).

**Figure 1.1:** Comparison of refraction phenomena, for an electromagnetic wave (McKenna [2014]) and for shock waves Abd-El-Fattah et al. [1976]).

gas-gas interface when it comes to internal combustion engines. In the present report, we have only studied gas-gas interface which are called slow-fast. It means that the acoustic impedance of the first (incident) gas, defined as  $(\rho a)$  where  $\rho$  is the density of the gas and  $a$  is the speed of sound [Henderson, 1970], is lower than that of the second (transmitted) gas. As for Snell-Descartes law for light refraction, the ratio of these two impedances have a huge impact on the refraction pattern [Henderson, 1966, 1970, Nourgaliev et al., 2005].

- **The shock wave:** a shock wave is a discontinuity surface in a compressible flow [Anderson, 2017]. For instance, in figure 1.1 (b), the straight line labelled "i" is the incident shock wave. State variables such as pressure, temperature or density of the flow undergo a jump whose amplitude depends on the Mach number of the flow and the specific heat ratio of the phase. The shock-jump equations are recalled in appendix A.2.
  - **The Prandtl-Meyer expansion:** unlike shock waves, expansion waves appear when the compressible flow has to adapt to a convex change of direction: discontinuity is not necessary [Anderson, 2017]. In such expansions, the flow is isentropic and Prandtl-Meyer equations, recalled in appendix A.3 describe the evolution of pressure, temperature and density.
- Shocks and expansions are the two fundamental elements that make up the more complex refraction patterns.

We have to keep in mind three important concepts while studying shock wave refraction:

- Mach number and strength of a shock are directly related through the jump relation A.1. For a given medium, a shock can be represented by its Mach number  $M = u/a$  (where  $u$  is the speed of the shock) or its strength  $\xi = P_2/P_1$  (where  $P_2$  is the pressure downstream and  $P_1$  the pressure upstream) without ambiguity. Note that  $\chi = 1/\xi$  may be used for convenience.
- Mach number, angle of incidence of the shock and angle of deflection of the flow behind the shock are three dependent parameters [Anderson, 2017].
- The interface is a contact surface: the flow behind the waves is parallel to the interface on each side of it and pressures on both sides are equal. This assertion means that the refraction structure highly depends on boundary conditions, which can cause irregularity.

Along with these basic concepts and definitions, we need some fundamental analysis tools to have a full understanding of the topic. Then it will be possible to start studying refraction structures and the transitions between them.

- **Polar diagrams:** while studying compressible flows, polar diagrams become useful for graphical understanding of the phenomena under study [Ben-Dor, 2007]. These diagrams (see next section) plot the deflection angle of the flow across the wave against the strength of the wave, whether it is a shock wave or an expansion wave. Because these two variables, along with the Mach number of the incident flow, fully define the wave, it is possible to determine the state of a flow by finding the intersection of two polars (figures 1.2 and 1.4). Equations A.6 and A.10 describe how to plot such polar diagrams.
- **Lagrangian formulation:** one way to determine whether ignition takes place is to theoretically isolate a fluid particle and to follow the evolution of its state variables. This formulation of the problem is called *Lagrangian formulation*. As we will explain it later, the position of the fluid particle under study has an impact on the delay of detonation.
- **Computational Fluid Dynamics (CFD):** the equations of fluid dynamics do not typically have closed-form solutions unless very strong simplifying assumptions are made. Computational fluid dynamics has proved to be an important tool to tackle problems that involve compressible flows. Here, we use CFD results from Nourgaliev et al. and Dr. Gallier, from ArianeGroup, to study the different refraction patterns, as well as to illustrate and corroborate our analyses.

## Regular refraction patterns

A refraction structure is called *Regular* when it is composed of three waves: incident, reflected and transmitted, that intersect at a single point referred to as “triple point”. Given a planar shock wave strength and interface angle, we can determine the speed at which the triple point propagates along the interface [Anderson, 2017]. At slow-fast interfaces, regular refraction structures usually occur at small angles of incidence [Jahn, 1956, Abd-El-Fattah et al., 1976, Abd-El-Fattah and Henderson, 1978] although the strength of the shock can influence the nature of the reflected shock.

Regarding polar diagrams, each wave has its own polar. The incident and the transmitted wave polars start at the origin of the graph as a shock of zero strength results in no flow deflection. However, the reflected wave polar starts at the point  $(\delta_1; \xi_i)$ , where  $\delta_1$  is the deflection behind the incident shock and  $\xi_i$  is its strength (see equations A.1 and A.6). A new starting point shows that the flow has been modified before it encounters the reflected shock.

The position of the intersection between reflected wave polar and transmitted wave polar determines whether the reflected wave is a shock or an expansion. It also gives the strength and deflection of the transmitted shock wave. This assertion comes from the pressure and deflection equilibrium that exist between each side of the interface (see previous subsection).

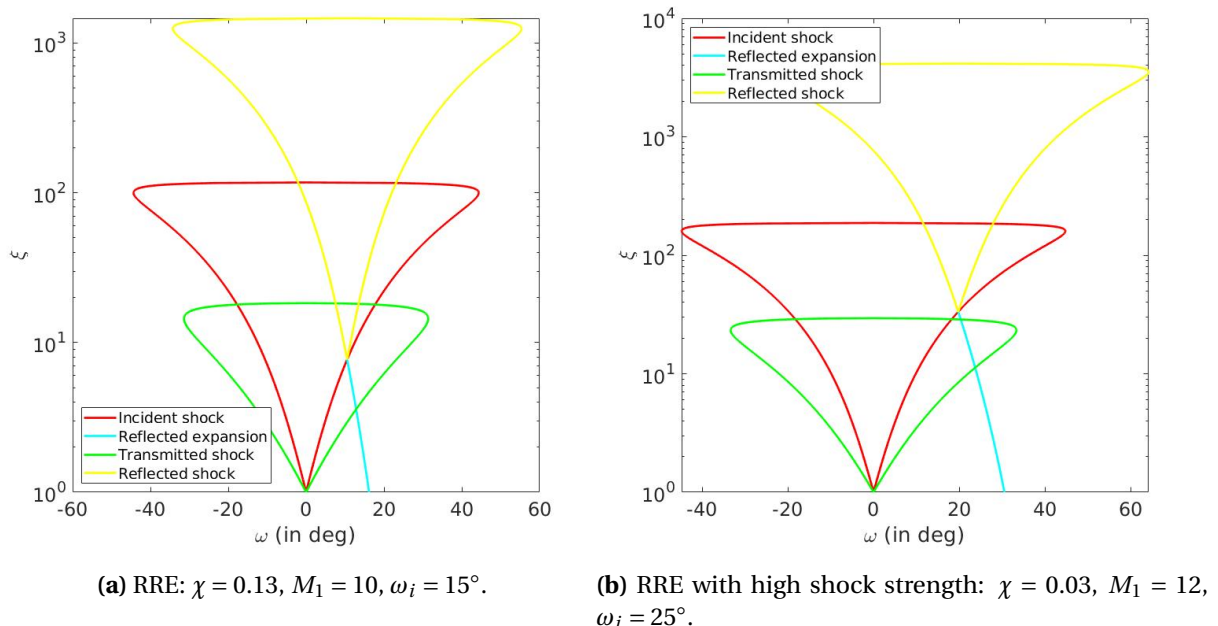
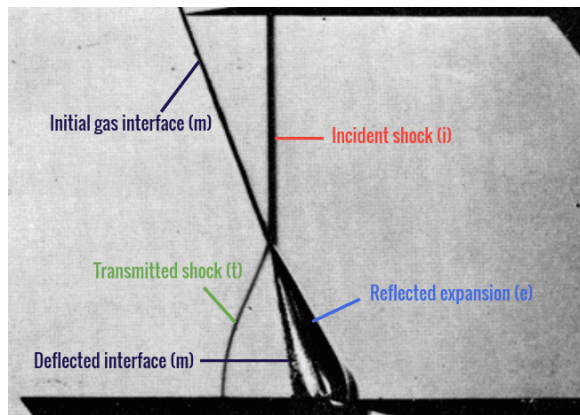


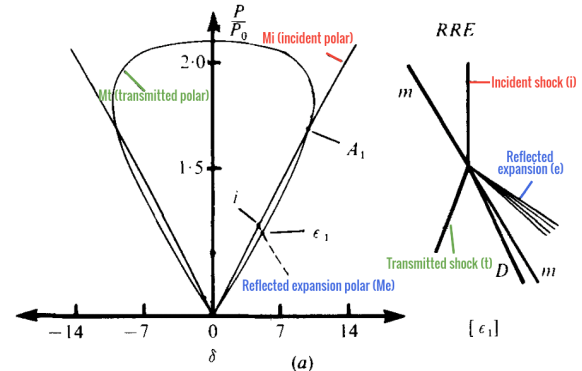
**Figure 1.2:** Polar diagram for *Regular refraction with reflected Expansion* structure.

In figure 1.2 (a), the transmitted shock polar intersects the cyan line: the reflected wave is thus an expansion and the intersection point determines pressure and deflection of the flow across the transmitted wave. This refraction structure is called a *Regular Refraction with reflected Expansion* (RRE, see figure 1.3). Another situation occurs when the incident shock is stronger: in figure 1.2 (b), transmitted polar has two intersection points with the reflected

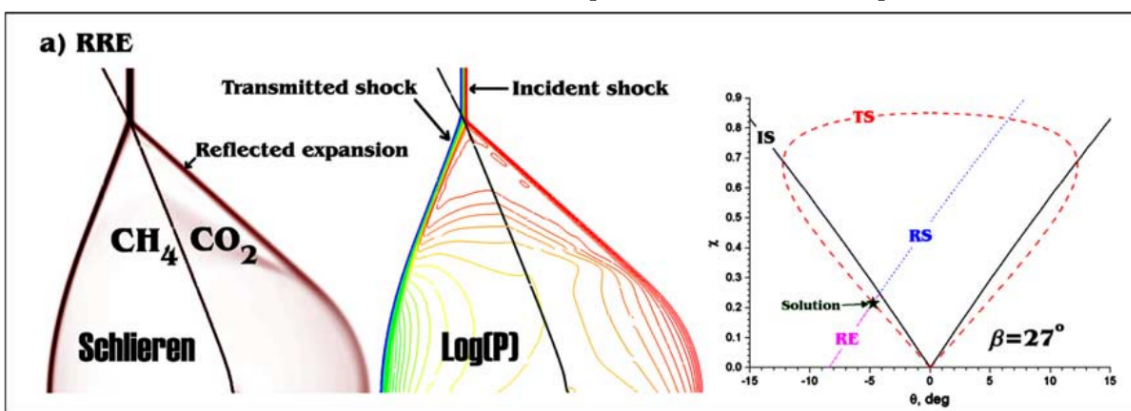
expansion polar. Experiments show that the weakest solution (the one which minimizes entropy) is observed, unless very specific experimental conditions are employed [Abd-El-Fattah et al., 1976].



(a) Schlieren photograph  
 $\omega_i = 15^\circ, \chi = 0.5$ .



(b) Polar diagram - Schematic ( $\omega_i = 31^\circ, \chi = 0.78$ ):  $A_1$  intersection point between the incident polar and the transmitted polar;  $i$  coordinates of the incident shock;  $e_1$  intersection point between the reflected expansion polar and the transmitted polar.



(c) Schlieren simulation - Log(P) isocontour - Polar diagram ( $\omega_i = \beta = 27^\circ, \chi = 0.78$ ): IS incident shock polar; TS transmitted shock polar; RS reflected shock polar; RE reflected expansion polar.

**Figure 1.3:** Illustration of *Regular Refraction with reflected Expansion* structure, from Abd-El-Fattah et al. [1976], Abd-El-Fattah and Henderson [1978], Nourgaliev et al. [2005].

We can make the same comment for figure 1.4: the transmitted shock polar intersects the reflected shock polar and, even if two solutions are theoretically possible, only the weakest phenomenon occurs. This time, we have a *Regular Refraction with Reflected shock* (RRR, see figure 1.5).

As the angle of incidence of the incident shock increases, the starting point of the reflected wave polar moves away from the origin, until an intersection between the transmitted and a reflected wave polar is not longer possible (figures 1.6 (a) and (b); the refraction has become *Irregular*).

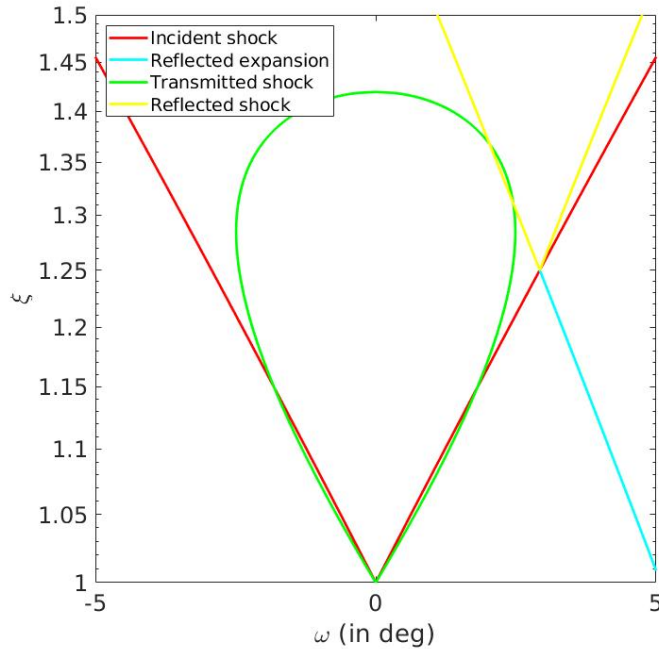


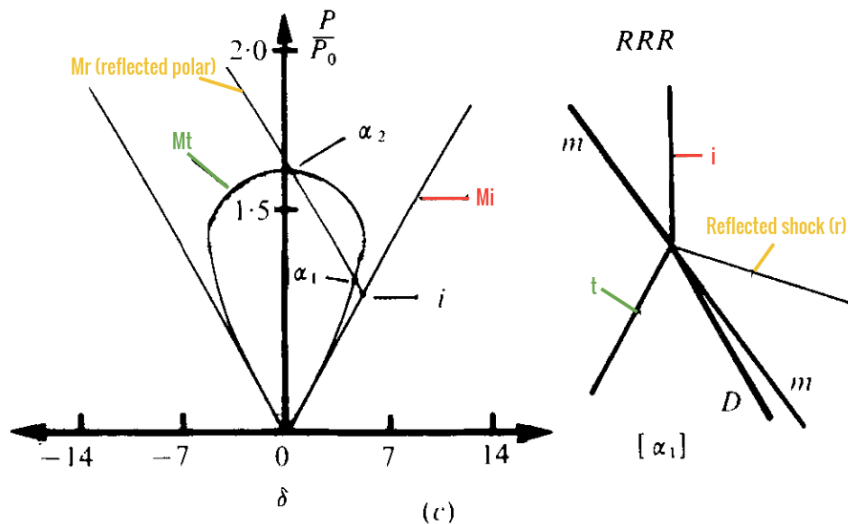
**Figure 1.4:** Polar diagram for *Regular Refraction with Reflected shock* structure:  $\chi = 0.80$ ,  $M_1 = 3$ ,  $\omega_i = 21.5^\circ$ .

## Irregular refraction patterns

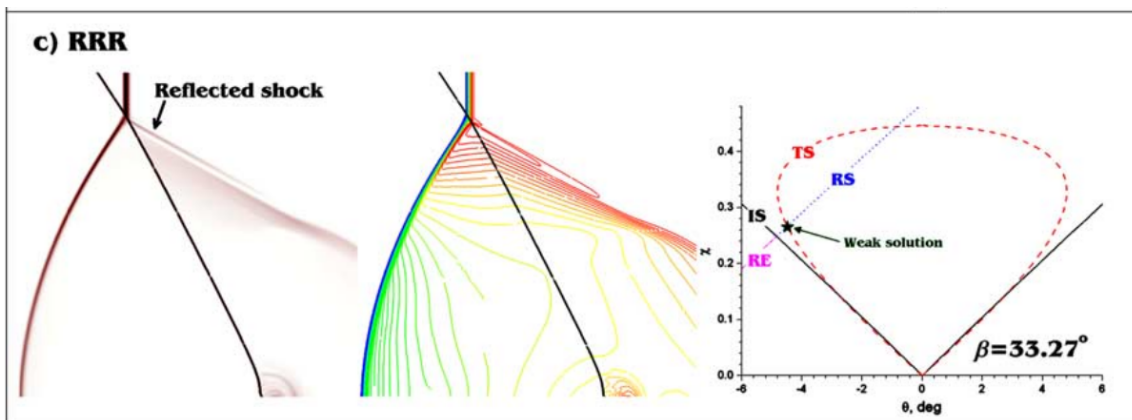
With increasing angle of incidence, the refraction pattern becomes irregular, a "triple point" no longer exists as the transmitted shock travels ahead of the incident shock; a new shock and expansion waves appear. At a sufficiently small angle of incidence, the transmitted shock travels at almost the same speed as the incident shock and the refraction point (intersection of incident and reflected waves) is located on the interface [Nourgaliev et al., 2005]. This refraction pattern is called a *Bound Precursor Refraction* (BPR, see figure 1.7). A slight discrepancy can be observed between the schematic in figure 1.7 (b) on the one hand and the schlieren photograph (a) and the simulation (c) on the other hand. The existence of a fourth wave, which is an expansion, will be discussed later.

As the angle of incidence further increases, the transmitted shock has a significantly higher velocity and is locally refracted back in the slow phase [Nourgaliev et al., 2005], in the form of an evanescent wave, called *s*-wave by Nourgaliev et al. or *j*-wave by Abd-El-Fattah and Henderson. This *j*-wave interacts with the incident shock to form a *k*-wave that connects the refraction point to the interface. The interaction between the *k*-wave and the interface creates an expansion called *e*-wave. This structure is called a *Free Precursor Refraction* (FPR, see figures 1.8).

In some configurations, it is possible to observe a *Free precursor von-Neumann Refraction* (FNR, see figures 1.9). The *j*-wave becomes stronger and the *e*-wave in FPR causes a small reflection near the stem of the *k*-wave, referred to as *von-Neumann reflection*. Abd-El-Fattah



(a) Polar diagram - Schematic ( $\omega_i = 36^\circ$ ,  $\chi = 0.78$ ):  $\alpha_{1,2}$  intersection points between the reflected shock polar and the transmitted polar;  $i$  coordinates of the incident shock;  $m$  initial position of the gas interface;  $D$  deflected gas interface.



(b) Schlieren simulation - Log( $P$ ) isocontour - Polar diagram ( $\omega_i = \beta = 33.27^\circ$ ,  $\chi = 0.78$ ):  $IS$  incident shock polar;  $TS$  transmitted shock polar;  $RS$  reflected shock polar;  $RE$  reflected expansion polar.

**Figure 1.5:** Illustration of *Regular Refraction with Reflected shock* structure, from Abd-El-Fattah and Henderson [1978], Nourgaliev et al. [2005].

and Henderson reported it for the first time and speculated that experimentally distinguishing FPR from FNR may be difficult.

With a further increase of the angle of incidence, the refraction point splits in two intersection points where von-Neumann reflections are observed. This *Twin von-Neumann Refraction* (TNR, see figure 1.10) is characterized by a Mach stem ( $n$ ) that connects the two intersection points. The incident and reflected shocks meet at the first point, along with a first slip surface  $SS1$  and the  $n$ -wave. The  $j$ -wave and the  $k$ -wave meet at the second point, along with the stem of the  $n$ -wave and a second slip-surface  $SS2$ . Each intersection point moves along a straight line that forms a given angle with the initial gas interface, labeled  $m$  in figure 1.10 (b).

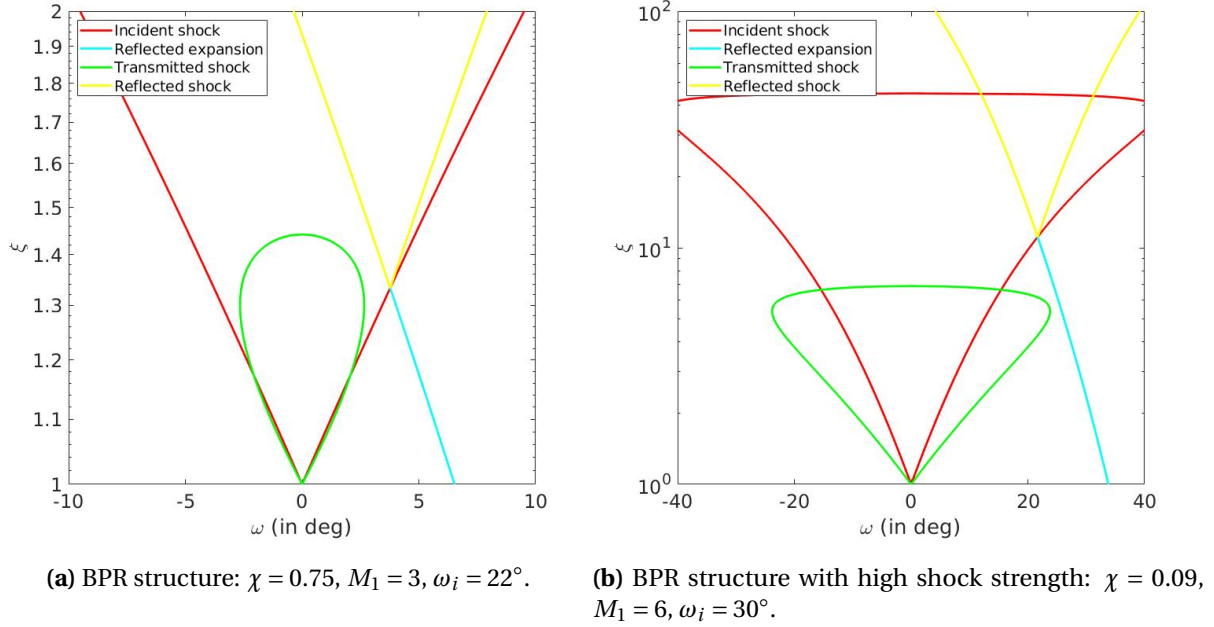
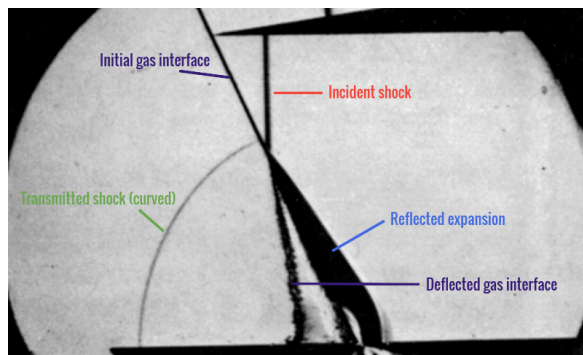


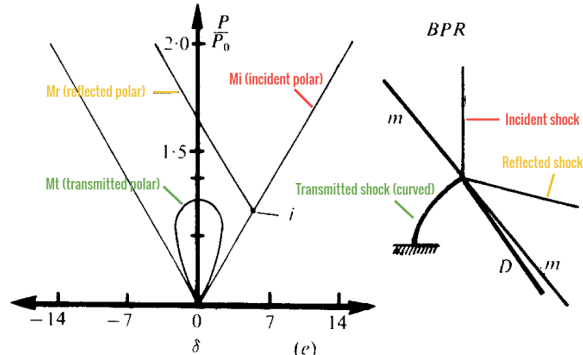
**Figure 1.6:** Polar diagram for *Bound Precursor Refraction* structure.

Finally, as the angle of incidence of the incident shock becomes larger, the Mach number downstream of it approaches unity and the reflected shock weakens to become a Mach wave. In this last structure, there is no reflected shock, anymore, neither *n*-wave or *e*-wave: the incident shock is slightly curved and only the second von-Neumann reflection is present. [Abd-El-Fattah and Henderson](#) seem to have observed the *Lambda-Shock Refraction* (LSR, see figure 1.11) for the first time. They also noticed that the LSR structure was the first one to lose self-similarity.

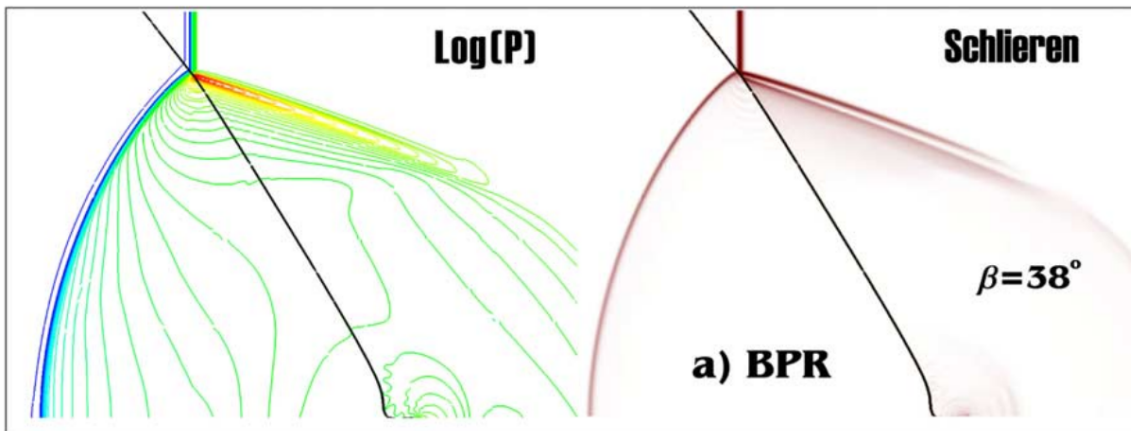
Even if, [Jahn](#) attempted to determine transition criteria between the different refraction structures, [Abd-El-Fattah and Henderson](#) were the first to propose a detailed description of each structure and a criterion for transitions. Both [Jahn](#) and [Abd-El-Fattah and Henderson](#) provided transition maps, also called regime diagrams. The main advantage of this representation is its convenience, as it summarizes the refraction types using two parameters in a single diagram. The refraction structure, when the incident shock encounters a given gas interface, depends only on the shock strength,  $\chi$  (or its Mach number), on the angle of incidence,  $\omega$ , and on the ratio of specific heats of each phase. Thus each structure has a defined domain of existence in the regime diagram and the distribution of domains is always valid, provided the properties of the interface studied remain constant.



(a) Schlieren photograph  
( $\omega_i = 25^\circ$  (measured),  $\chi = 0.5$ ).



(b) Polar diagram - Schematic (unknown angle  $\omega_i$ ,  $\chi = 0.78$ ):  $i$ :  $i$  coordinates of the incident shock;  $m$ : initial position of the gas interface;  $D$ : deflected gas interface.



(c) Log(P) isocontour - Schlieren simulation ( $\omega_i = \beta = 38^\circ$ ,  $\chi = 0.78$ ).

**Figure 1.7:** Illustration of *Bound Precursor Refraction* structure, from Abd-El-Fattah et al. [1976], Abd-El-Fattah and Henderson [1978], Nourgaliev et al. [2005].

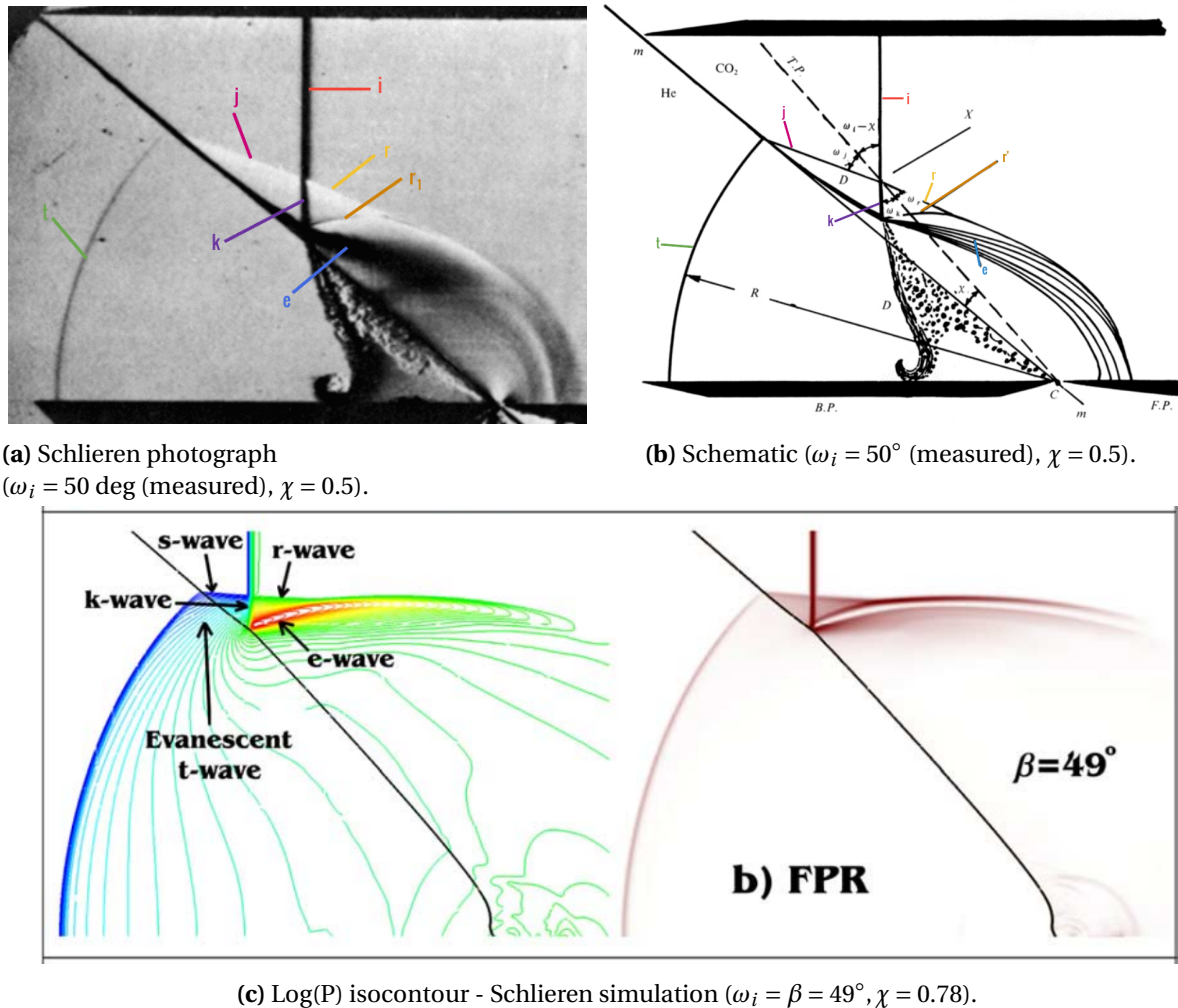


**Figure 1.8:** Illustration of *Free Precursor Refraction* structure, from Abd-El-Fattah et al. [1976], Nourgaliev et al. [2005]:  $i$  incident shock;  $r$  reflected shock;  $t$  transmitted shock;  $j$  or  $s$   $j(s)$ -shock, refracted back from  $t$ -shock;  $k$   $k$ -shock result of the interaction between  $i$ -shock and  $j$ -shock;  $r_1$   $r_1$ -shock and  $e$   $e$ -wave (expansion) results of the interaction between  $k$ -shock and the interface.

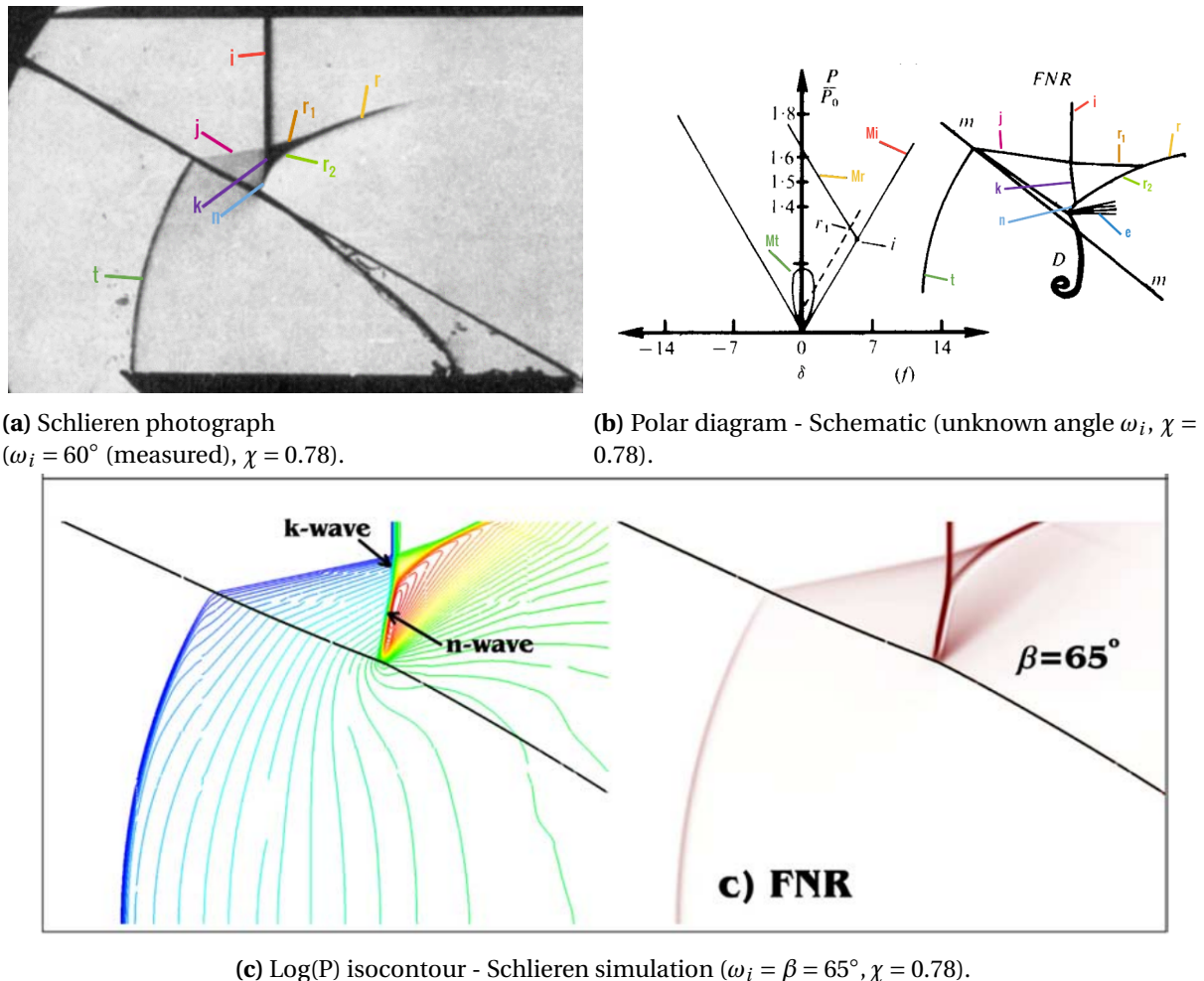


**Figure 1.9:** Illustration of *Free von-Neumann Refraction* structure, from Abd-El-Fattah et al. [1976], Abd-El-Fattah and Henderson [1978], Nourgaliev et al. [2005]: *i* incident shock; *r* reflected shock, fusion of *r*<sub>1</sub> and *r*<sub>2</sub>; *t* transmitted shock; *j* j-shock, refracted back from *t*-shock; *r*<sub>1</sub> reflected shock from von-Neumann reflection; *k* k-shock result of the interaction between *i*-shock and *j*-shock; *n* stem of *k*-shock; *e* e-wave (expansion) results of the interaction between *n*-stem and the interface; *r*<sub>2</sub> compression wave created by strengthening *e*-wave.

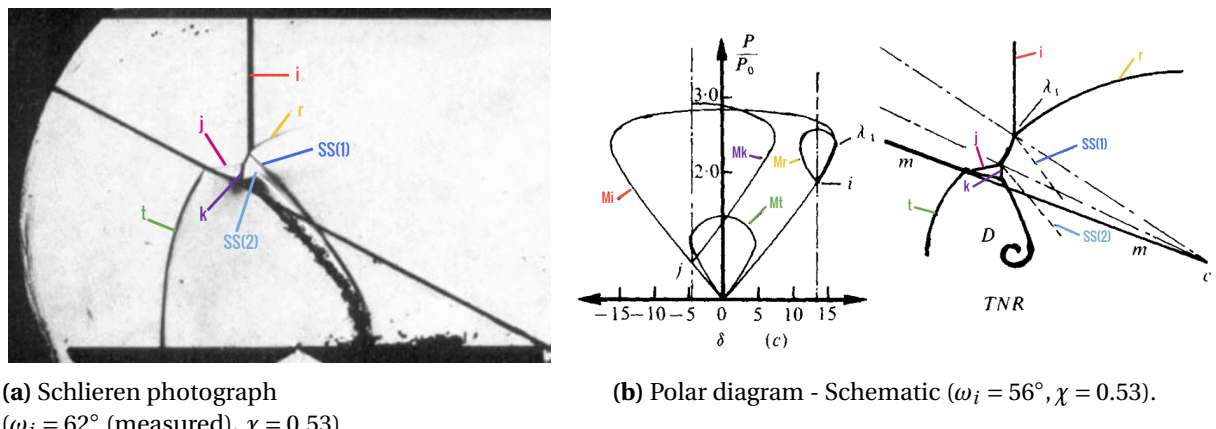
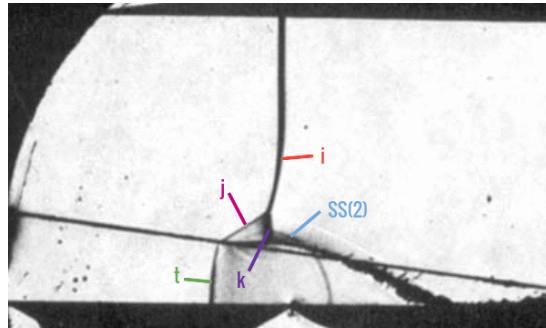
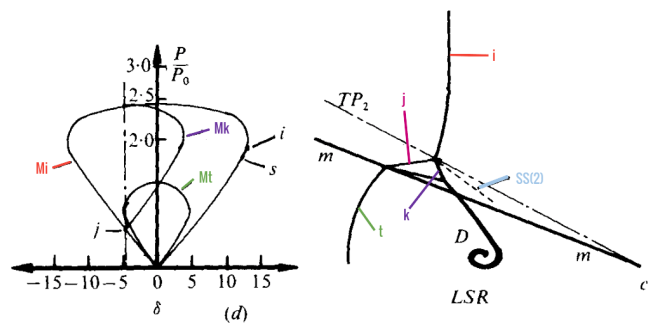


**Figure 1.10:** Illustration of *Twin von-Neumann Refraction* structure, from Abd-El-Fattah and Henderson [1978]: *i* incident shock; *r* reflected shock; *SS1* slip surface from first von-Neumann reflection; *t* transmitted shock; *j* j-shock, refracted back from *t*-shock; *r*<sub>1</sub> reflected shock; *k* k-shock result of the interaction between *i*-shock and *j*-shock; *SS2* slip surface from second von-Neumann reflection.



(a) Schlieren photograph  
 $\omega_i = 81^\circ$  (measured),  $\chi = 0.53$ .



(b) Polar diagram - Schematic ( $\omega_i = 63^\circ$ ,  $\chi = 0.53$ ).

**Figure 1.11:** Illustration of *Lambda Shock Refraction* structure, from Abd-El-Fattah and Henderson [1978]:  $i$  incident shock;  $t$  transmitted shock;  $j$   $j$ -shock, refracted back from  $t$ -shock;  $k$   $k$ -shock result of the interaction between  $i$ -shock and  $j$ -shock;  $SS2$  slip surface from second von-Neumann reflection.

## 1.2 MAP OF THE REFRACTION DOMAINS FOR THE CO<sub>2</sub>-CH<sub>4</sub> INTERFACE

Abd-el-Fattah and Henderson studied CO<sub>2</sub>-CH<sub>4</sub> interfaces [Abd-El-Fattah and Henderson, 1978] and gave theoretical criteria for some of the transitions between structures. Note that interfaces are labeled as follow : slow phase - fast phase, separated by a dash to symbolize the interface. While carrying out experiments, they divided the plane into three parts: (i) very weak, (ii) weak and (iii) strong zones, corresponding to the three sets of experiments using shock strengths of  $\chi = 0.78, 0.53$  and  $0.18$ . Their theory predicts well the structures obtained experimentally, as shown in Fig. 13 of Abd-El-Fattah and Henderson [1978]. Furthermore, Nourgaliev et al. used an “Adaptative Characteristic-based Matching” method to compute the refraction phenomenon for the same shock strengths.

Previous work by de Gouvello allowed to explicitly delineate the boundaries between the different structures, as shown in figure 1.12. It is then possible to compare these boundaries for the CO<sub>2</sub>-CH<sub>4</sub> interface and to compare with Henderson’s results [Abd-El-Fattah and Henderson, 1978].

The criteria used to plot figure 1.12 can be found in Appendix B. The comparison with Fig. 13 from Abd-El-Fattah and Henderson [1978] is satisfactory, except for the FPR-TNR transition; potential sources of discrepancies are discussed later. Comparing with Nourgaliev et al.’s simulations, results are also in agreement. Even if they did not cover the entire regime diagram, the similitude between the experimentally obtained structures and those theoretically predicted is promising.

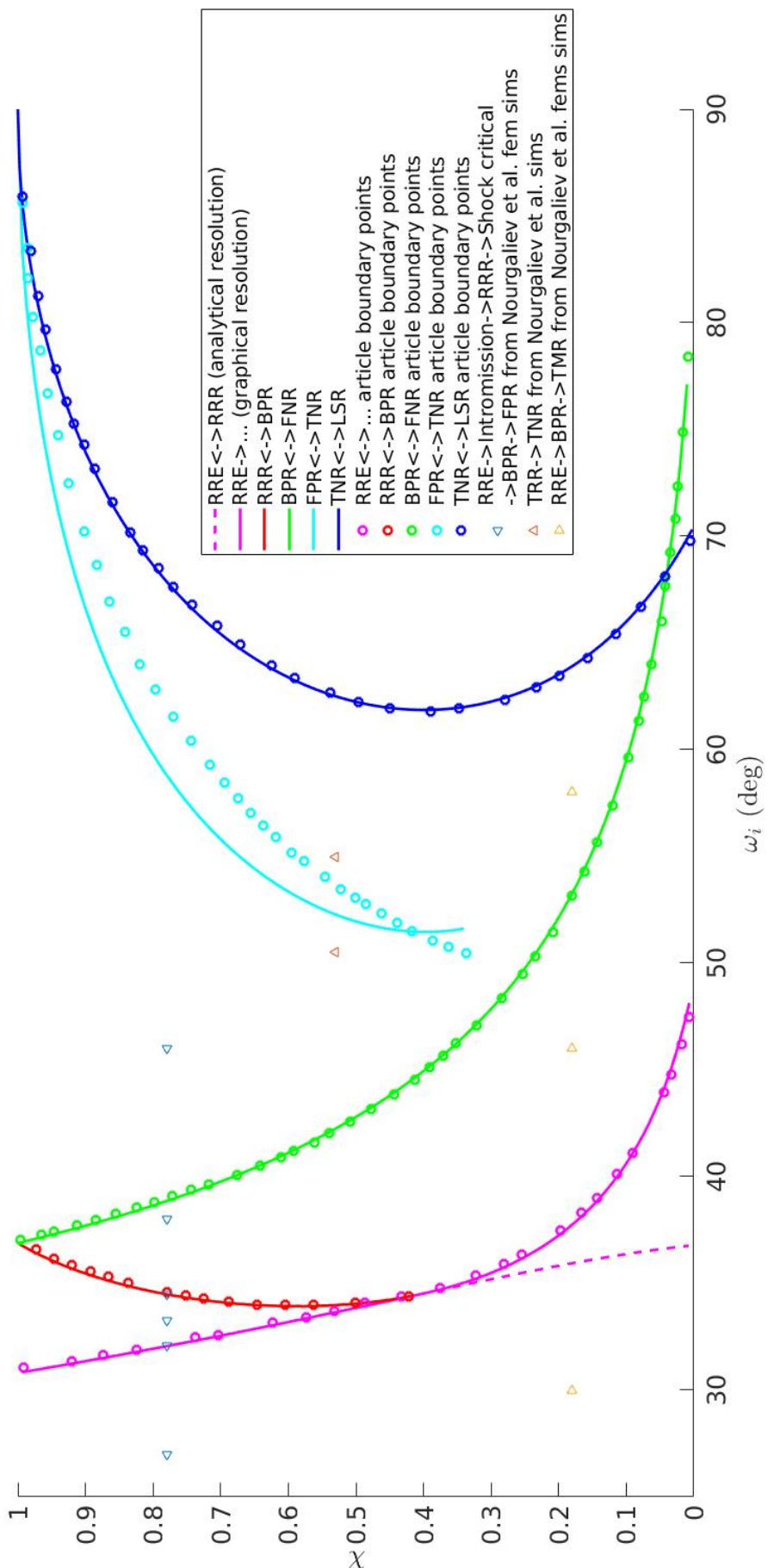


**Figure 1.12:** Comparative regime diagram for the  $\text{CO}_2\text{-CH}_4$  interface, from de Gouvello [2019]. Solid lines represent the criteria computed;  $\circ$  represent the digitized theoretical boundaries from figure 13 in [Abd-El-Fattah and Henderson, 1978];  $\Delta$  represent the simulations from Nourgaliev et al. [2005].

## Discrepancies analysis and possible improvements

Discrepancies on the FPR-TNR transition are evident in figure 1.12. They were explained by the influence of the membrane used in the experiments (i.e. its inertia) [de Gouvello, 2019]. In fact, Abd-El-Fattah et al. developed a theory called “piston theory” in order to determine the velocity of the transmitted shock in a given structure, which we outline next.

**Piston theory** Let  $V_p$  be the velocity of a piston moving in a shock tube and  $V_w$  be the velocity of the shock created by the piston compressing the gas.  $\gamma_g$  is the specific heat ratio of the gas at hand.



**Figure 1.13:** Schematic for the piston theory: in red the considered shock with velocity  $V_w$ , in white, the fictive driving piston with velocity  $V_p$ .  $a_{1,2}$  is for the speed of sound respectively in the undisturbed and disturbed gases.

$V_p$  and  $V_w$  are related with the following equation

$$V_p = \frac{2}{\gamma_g + 1} \frac{V_w^2 - a_1^2}{V_w}$$

Abd-El-Fattah et al. have experimentally observed that, whatever the refraction structure, the incident shock and the transmitted shock can be approximated with the same piston velocity  $V_p$ . Thus, the following equality is obtained:

$$V_p = \frac{2}{\gamma_I + 1} \frac{V_i^2 - a_1^2}{V_i} = \frac{2}{\gamma_{II} + 1} \frac{V_t^2 - a_5^2}{V_t}$$

where  $V_i$  and  $V_t$  are the **normal** velocities of the incident and the transmitted shock, respectively;  $\gamma_{I,II}$  are the specific heat ratio of phase I and II respectively;  $a_1$  is the speed of sound in the undisturbed gas for the incident shock (i.e. zone (1) in figure 2.2) and  $a_5$  is the speed of sound in the undisturbed gas for the transmitted shock (i.e. zone (5) in figure 2.2).

After some algebra, Abd-El-Fattah et al. derived an expression for the velocity of the transmitted shock  $V_t$ , as a function of the incident shock, independent of  $\omega_i$ , the angle between the incident shock and the interface.

$$V_t = \frac{1}{2} \left( b + \sqrt{b^2 + 4a_5^2} \right) \text{ where } b = \frac{\gamma_{II} + 1}{\gamma_I + 1} \frac{V_i^2 - a_1^2}{V_i}$$

**Membrane inertia** Unfortunately, assuming similar piston velocities for the incident and the transmitted shocks is not valid for strong shocks. As shown in Fig.8 from [Abd-El-Fattah and Henderson \[1978\]](#), the real  $V_t$  depends on  $\omega_i$ . The explanation given by [Abd-El-Fattah et al.](#) relates to the membrane they used to keep gases separated before interaction with the incident shock. The inertia of the membrane has an effect on the transmitted piston velocity but the authors did not explicitly detail this effect. The only indication given in section 4.4 of [Abd-El-Fattah et al. \[1976\]](#) is that the piston velocity of the transmitted shock is lower than the theoretical value. However, correcting the transmitted shock velocity by a constant factor for all  $(\chi, \omega_i)$  values is not satisfactory, as shown by the dashed cyan line in figure 1.15. The transition boundary is only translated but not re-adjusted.

We tried to find a better model for this boundary by assuming that the ratio of piston velocities depends on the angle of incidence. This assumption only affects the value of the parameter  $b$ . We approximated the experimental data provided by [Abd-El-Fattah et al.](#) ([Fig. 8 \(b\)](#)) with a numerical optimization method. We defined the problem to solve as follows and we used MATLAB non-linear least-squares solver (premade function) to fit the experimental curve. The function to minimize is:

$$f(x_1, x_2, x_3) = \frac{V_t}{V_i}(x_1, x_2, x_3) - \frac{V_{t(exp)}}{V_{i(exp)}} \quad (1.1)$$

where  $V_{t(exp)}/V_{i(exp)}$  are the experimental points. The three parameters to optimize act in the expression of  $b$ :

$$b = (x_1 \omega^2 + x_2 \omega + x_3) \frac{\gamma_{II} + 1}{\gamma_I + 1} \frac{V_i^2 - a_1^2}{V_i}$$

The result of the minimized problem 1.1 is plotted in figure 1.14.

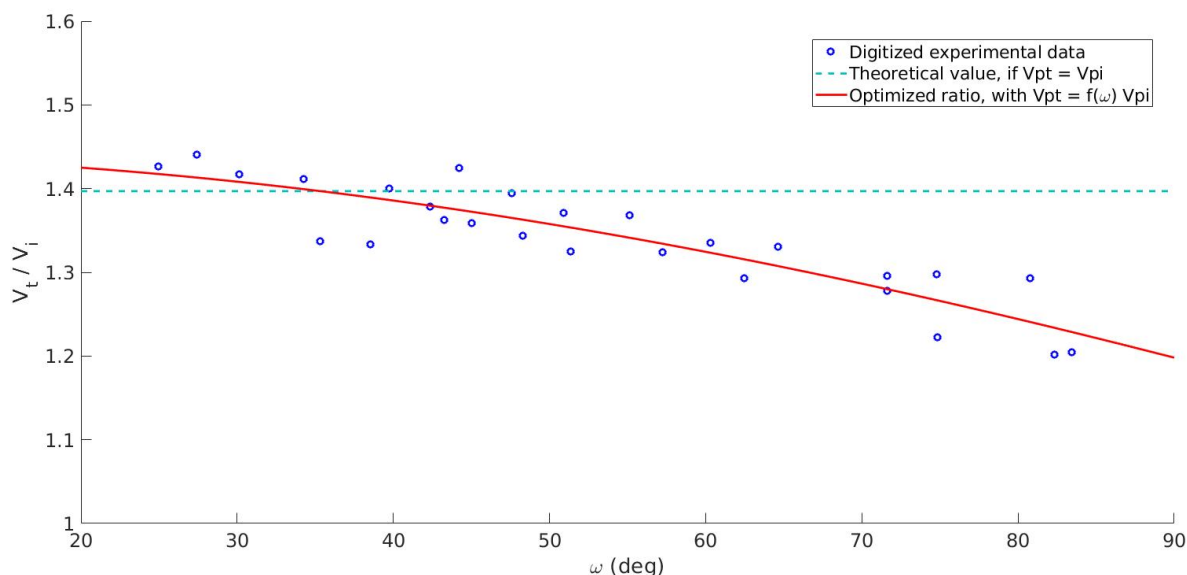


**Figure 1.14:** Optimization of the ratio of piston velocities, based in figure 8b from [Abd-El-Fattah et al. \[1976\]](#).

The values of the three parameters  $x_1$ ,  $x_2$  and  $x_3$  were used to plot the dashed-dotted cyan line in figure 1.15. The result obtained is satisfactory for relatively weak shocks: as the incident shock becomes stronger, it becomes faster and our method fails. Furthermore, note that the methodology proposed requires experimental data, which is only available for the CO<sub>2</sub>-CH<sub>4</sub> interface considered. As of now, we have not been able to find a valid theory to reproduce the FPR-TNR transition boundary included in [Abd-El-Fattah et al.](#), as more information is needed on the membrane model used by the authors. Even the explanations given by [Zeng and Takayama \[1996\]](#) are rather unclear to compute a boundary that could be applicable to arbitrary interfaces.

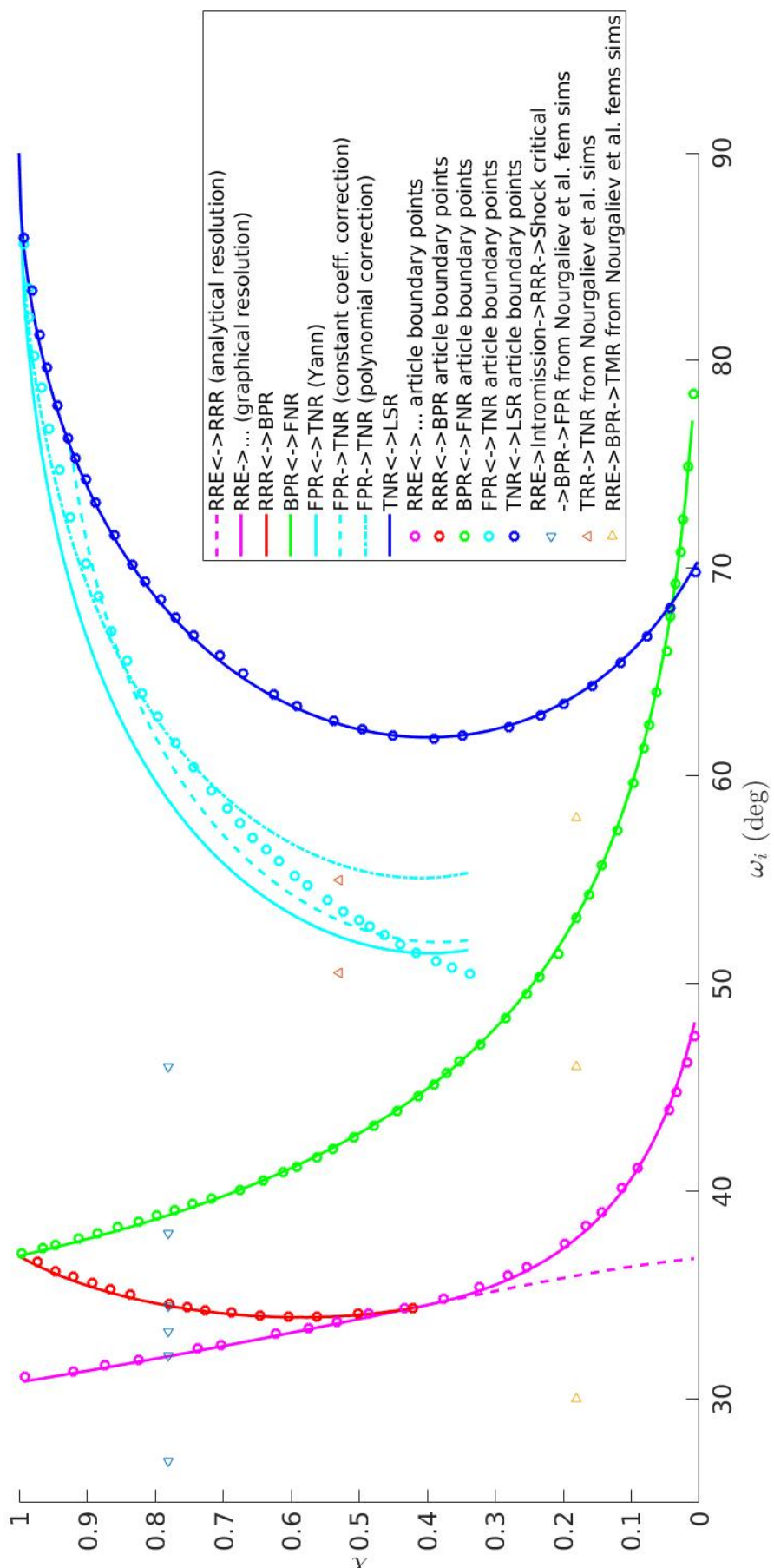


**Figure 1.15:** Comparative regime diagram for the  $\text{CO}_2\text{-CH}_4$  interface with correction for FPR-TNR transition. Solid cyan line represent the criteria computed in de Gouvello [2019]; dashed cyan line represent the first correction computed; dashed-dotted cyan line represent the polynomial correction.

### 1.3 MAP OF THE REFRACTION DOMAINS FOR THE AIR-CH<sub>4</sub> INTERFACE

The approach adopted by [Abd-El-Fattah and Henderson](#) is not new. [Jahn \[1956\]](#) attempted to map regime diagram by defining several critical angles for which the regular refraction theory no longer holds. Studying an Air-CH<sub>4</sub> interface, the author determined five critical angles of incidence that coincide with the boundaries found by [Abd-El-Fattah and Henderson](#). To define each critical angle, [Jahn](#) assumed a regular refraction could occur and analyzed whether physically meaningful results were obtained.

- (i)  $\alpha_e$  is defined as the angle for which it is no longer possible to satisfy both pressure and deflection conditions across the interface: solutions of the system of equations become imaginary. The structure thus needs to be irregular, that is to say to be composed of more than three waves.
- (ii)  $\alpha_i$  is the angle for which the transmitted shock acquires an angle of incidence greater than 90°. Let us refer to figure 2.2 to define the angular sectors (or zones) (1), (2), (3), (4) and (5). The contact surface condition on speed of flow across the interface imposes  $u_1 = u_5 \iff M_1 a_1 / \sin(\omega_i) = M_5 a_5 / \sin(\omega_t)$ . An expression for  $\alpha_i$  given by [Jahn](#) is thus  $\sin^2(\alpha_i) = [(M_1 a_1) / (M_5 a_5)]^2$ . In fact, the value  $M_5$  is fixed by pressure and deflection equilibrium across the interface. It means that, if the fixed value of  $M_5$  exceeds a critical value, then the computed  $\omega_t$  becomes imaginary: the assumption of regular refraction no longer holds.
- (iii)  $\alpha_j$  is the angle for which the transmitted wave can no longer be a straight shock. Its definition is quite similar to  $\alpha_i$  because it focuses on the same phenomenon: the inconsistency of the transmitted shock.  $\alpha_j$  can be defined by  $\sin(\alpha_j) = M_1 a_1 / a_5$  or by "if  $\omega_i = \alpha_j$  is reached then zone (5) becomes subsonic and *transmitted wave can no longer be a shock*" [[Jahn, 1956](#)].
- (iv)  $\alpha_a$  is defined as the angle of incident for which  $M_2 = 1$ , that is to say the reflected wave can no longer exist because the flow behind the incident shock becomes subsonic.
- (v)  $\alpha_A$  has a definition which is close to  $\alpha_a$  definition. Starting from  $\omega_i = 90^\circ$ , where  $M_2 < 1$ , and decreasing the angle of incidence, the critical angle  $\omega_i = \alpha_A$  is reached when  $M_2$  is sufficiently supersonic to permit the existence of the finite shock [[Jahn, 1956](#)].

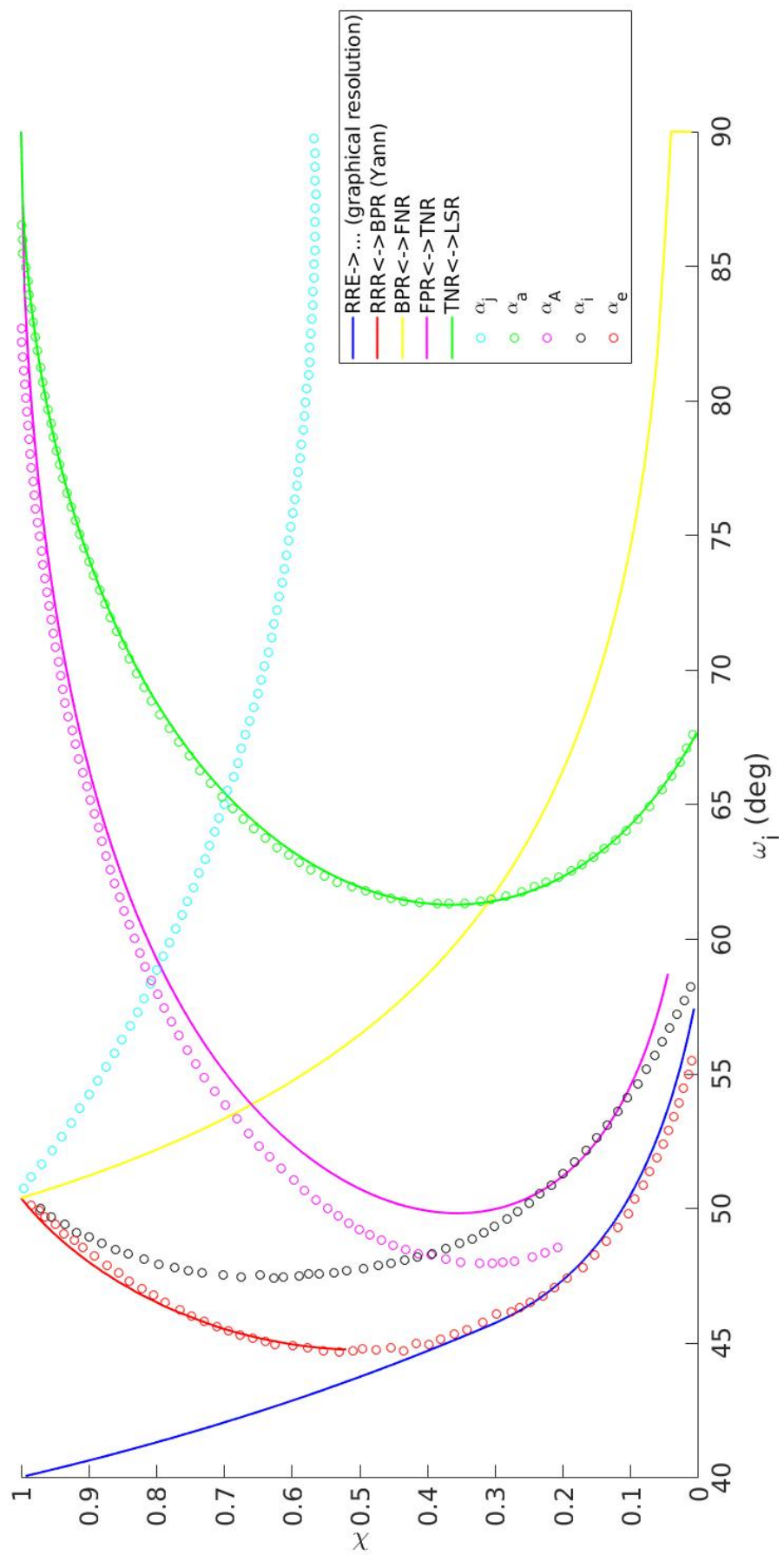


**Figure 1.16:** Comparative regime diagram for the Air-CH<sub>4</sub> interface. Solid lines represent the boundaries plotted with Henderson *et al.* criteria;  $\circ$  represent the digitized theoretical boundaries from figure 12 in Jahn [1956].

Several comments can be made concerning figure 1.16:

- (i) For the lowest angles of incidence, the critical angle  $\alpha_e$  predicts the transition from RRE or RRR structure to BPR pattern. [Jahn](#) highlighted that  $\alpha_e$  is supposed to be the first angle for which the refraction pattern becomes irregular;
- (ii) On the opposite side of the regime diagram, the critical angle  $\alpha_a$  perfectly matches the TNR-LSR transition. This is not surprising as [Abd-El-Fattah and Henderson](#) used the same definition for this boundary;
- (iii) Note that  $\alpha_j$  does not match any of [Abd-El-Fattah and Henderson](#)'s boundary; the same applies for the BPR-FNR boundary which is not matched by any of [Jahn](#)'s critical angles;
- (iv) The combination of the two critical angles  $\alpha_A$  and  $\alpha_i$  seem to approximate the FPR-TNR boundary. However, the definition of these two angles is very different: we cannot conclude that they both define the same boundary;

One possible option would be to take the distinction between FNR and FPR into account in [Abd-El-Fattah and Henderson](#)'s regime diagram. Further investigation would determine whether a boundary can be found in these domains and can justify the existence of the critical angles  $\alpha_A$  and  $\alpha_i$ . Mapping the regime diagram for Air-CH<sub>4</sub> interface 1.16 confirmed the validity of our approach.



## **2. Reactive interface: detonation initiation by refraction**

The present chapter is a second step in the study of detonation initiation within refraction structures. Setting a reactive gas as one of the two phases of the interface, we would like to determine the critical conditions for ignition to occur in the reactive phase by following the evolution of their thermodynamic state.

### **2.1 MAP OF THE REFRACTION DOMAIN FOR THE $\text{H}_2\cdot\text{O}_2\text{-He}$ INTERFACE**

To study the evolution of the state variables of the flow, it is necessary to determine the refraction structure that occurs for the conditions set. We have chosen to study a system with a  $\text{H}_2\cdot\text{O}_2\text{-He}$  interface, undisturbed phase I ( $\text{H}_2\cdot\text{O}_2$ ) having an initial temperature of  $T_1 = 600$  K and undisturbed phase II (He) having an initial temperature of  $T_5 = 1138$  K. The initial pressure of the undisturbed flow on both sides of the interface is  $P_1 = P_5 = 101325$  Pa. The regime diagram obtained is shown in figure 2.1.

Our method consists in choosing a value for the angle of incidence of the incident shock and exploring a number of shock strengths.

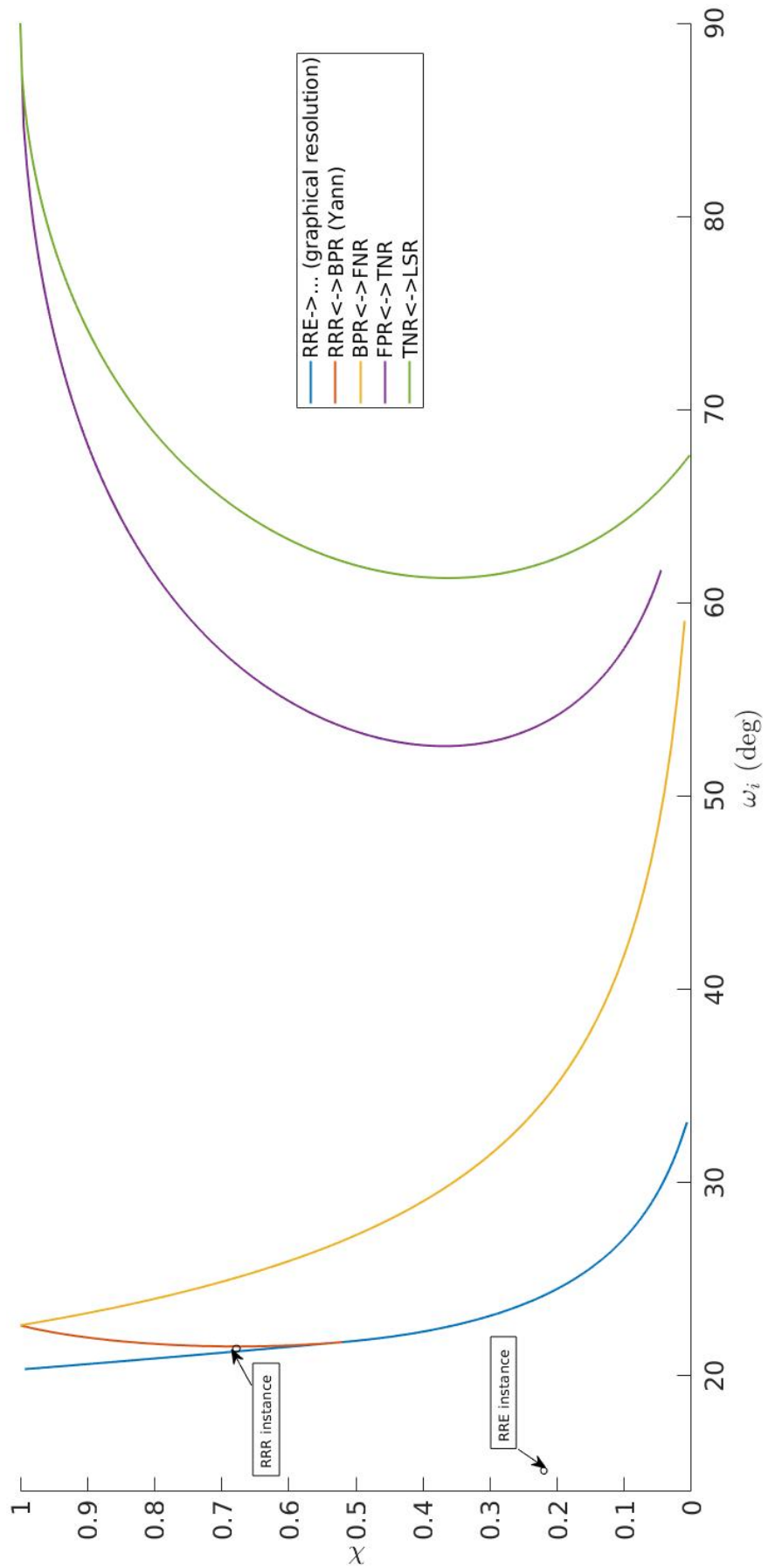


**Figure 2.1:** Regime diagram for the  $\text{H}_2\text{-O}_2\text{-He}$  interface.

## 2.2 PATH OF A LAGRANGIAN PARTICLE: GENERAL METHOD

A Lagrangian description of the problem provides a useful alternative to calculate pressure, temperature and specific volume of a fluid particle as it travels through the refraction structure. It is then easy to determine if this fluid particle ignites or not. To simplify our problem, let us assume both gases are calorically perfect, with constant specific heat ratios,  $\gamma_I$  and  $\gamma_{II}$ , and undergoing a reversible adiabatic process, i.e.  $PV^\gamma = \text{constant}$ . A Lagrangian particle crosses five different zones when it travels through a regular refraction: zone (1) is the undisturbed phase I; zone (2) is situated between the incident shock and the reflected wave; zone (3) is situated behind the reflected wave; zone (5) is the undisturbed phase II; zone (4) is the disturbed phase II (behind the transmitted shock). For irregular refraction, the partitioning becomes more complex: it will be detailed later.

Our method consists in selecting several fluid particles and to follow the evolution of their pressure  $P$ , temperature  $T$  and specific volume  $V$ . Knowing the evolution of their specific volume, we performed a chemical kinetics simulation to determine whether significant heat is released on the path of the chosen Lagrangian particles. This allowed us to find a critical Mach number for each particle from which ignition occurs.

## 2.3 DETONATION INITIATION FOR REGULAR PATTERNS

### Regular Refraction with reflected Expansion

To begin with, we chose to focus on the RRE structure, shown in figure 2.2. This schematic, not drawn to scale, is only a visual tool to understand the evolution along the path of a particle.

To go from zone (1) to zone (2), equations A.1 to A.6 allow to fully determine the state variables and the deflection of the flow. However, to go from zone (5) to zone (4), the angle of incidence of the transmitted shock is needed. That is why we used polar diagrams: the intersection of the transmitted shock polar and the reflected expansion polar gives  $\xi_t$  the pressure jump through the transmitted shock and  $\delta_t$  the deflection behind it.

Using the contact surface relationship ( $\delta_t = \delta_1 + \delta_2$ ), it is now possible to determine the deflection behind the expansion wave and to deduce the Mach number in zone (3),  $M_3$ , using equations A.7 to A.11.

**Evolution inside the expansion wave** Since the flow inside the expansion is isentropic and noting that it can be approximated by an infinite number of quasi Mach waves (infinitesimal discontinuities), we computed this evolution “step-by-step”. Taking the logarithmic derivative of the isentropic relationship between state variables yields:

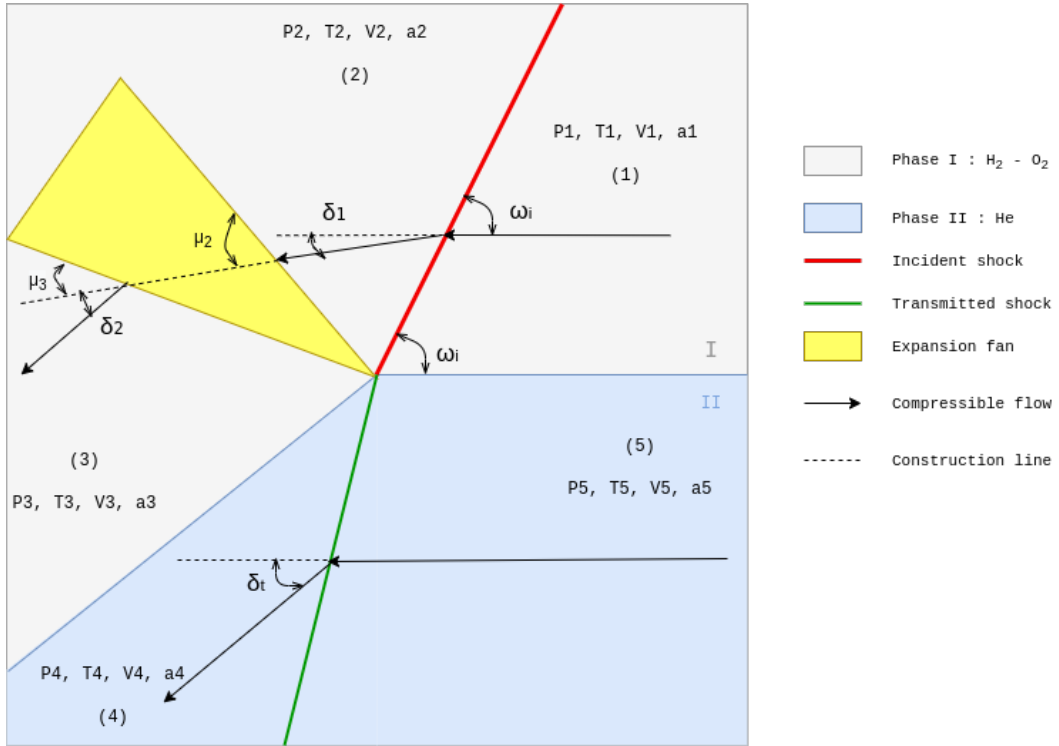


**Figure 2.2:** Notations, zones and angles for *Regular Refraction with reflected Expansion pattern*.

$$\begin{aligned}
 \frac{T_0}{T} &= 1 + \frac{\gamma_1 - 1}{2} M^2 \quad \Rightarrow \quad \frac{dT}{T} = -\frac{\frac{\gamma_1 - 1}{2} d(M^2)}{1 + \frac{\gamma_1 - 1}{2} M^2} \\
 \frac{P_0}{P} &= \left(1 + \frac{\gamma_1 - 1}{2} M^2\right)^{\frac{1}{\gamma_1 - 1}} \quad \Rightarrow \quad \frac{dP}{P} = -\frac{\frac{\gamma_1}{2} d(M^2)}{1 + \frac{\gamma_1 - 1}{2} M^2} \\
 \frac{V}{V_0} &= \left(1 + \frac{\gamma_1 - 1}{2} M^2\right)^{\frac{1}{\gamma_1 - 1}} \quad \Rightarrow \quad \frac{dV}{V} = \frac{\frac{\gamma_1}{2} d(M^2)}{1 + \frac{\gamma_1 - 1}{2} M^2}
 \end{aligned}$$

The subscript 0 is for stagnation properties (see section 7.5 in [Anderson \[2017\]](#)), which are constant because entropy is conserved. We chose a constant step of deflection for each Mach wave, which leads to a certain jump in squared Mach number  $d(M^2)$ : the evolution of state variables is then fully known.

**Gas dynamics results** To run our MATLAB program, we chose  $\omega_i = 14.5^\circ$  as angle of incidence and the strengths of shocks were  $\chi \in [0.01; 1] \iff M_{sh} \in [1; 2.95] \iff M_1 \in [4; 11.78]$ , where  $M_{sh}$  is the Mach number of the shock (equal to normal Mach number of the flow (see figure [A.1](#)).

Figures [2.3](#) and [2.4](#) show the evolution of a set of Lagrangian particle for a free-stream Mach number  $M_1 = 8$ , see “RRE instance” in figure [2.1](#). The schematic is now drawn to scale and the pressure, temperature and specific volume histories allow to observe the influence of the position of the particles.

The influence of the free-stream Mach number for a single particle is shown in figure [2.5](#).

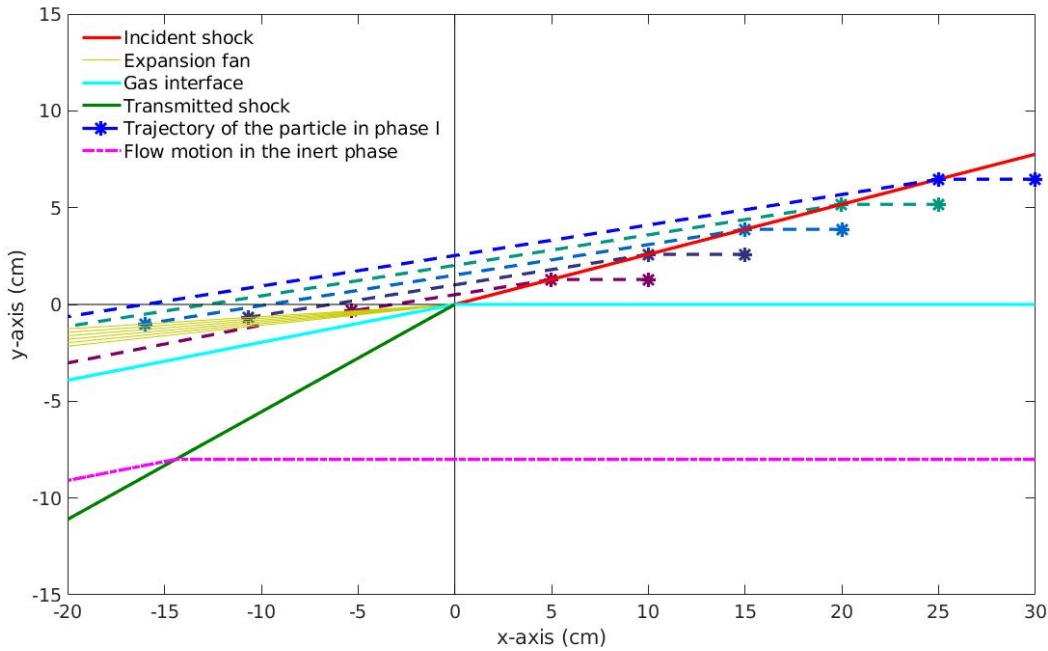


**Figure 2.3:** Regular refraction with reflected Expansion - Schematic of the path of several particles, at  $\chi = 0.22$ ,  $M_1 = 8$ ,  $\omega_i = 14.5^\circ$ .

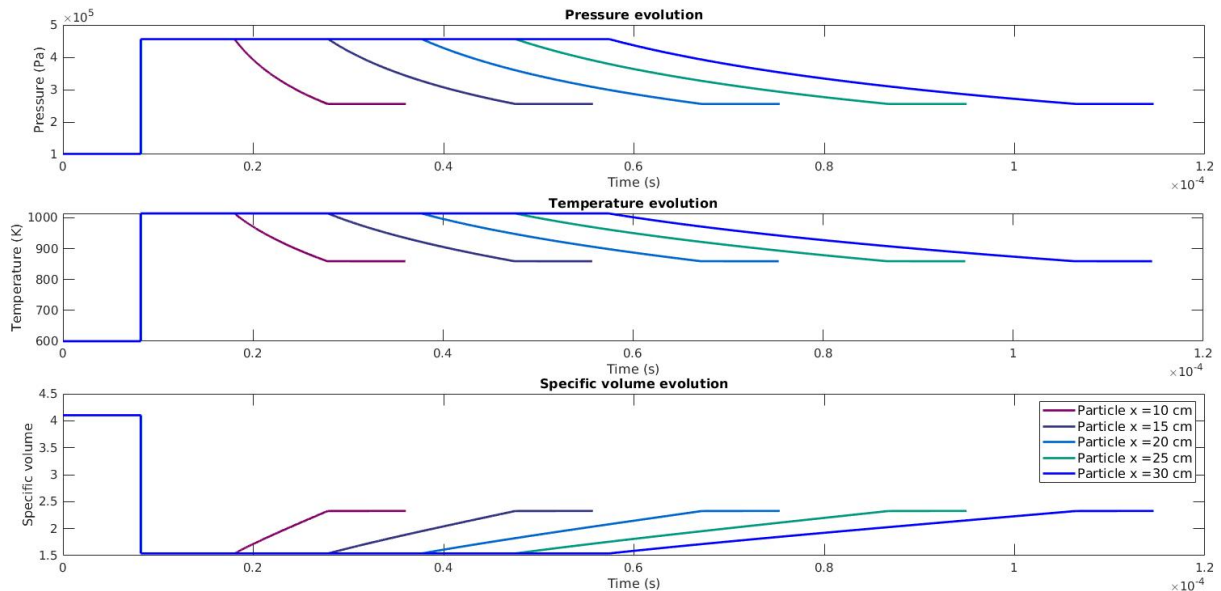


**Figure 2.4:** Regular refraction with reflected Expansion - Evolution of state variables for several particles, at  $\chi = 0.22$ ,  $M_1 = 8$ ,  $\omega_i = 14.5^\circ$ .

The pressure and temperature levels reached differ for each Mach number so it is relevant to search for the range of Mach numbers for which detonation occurs systematically.

**Reactive results** Running a CHEMKIN-II script allows to determine which conditions lead to ignition. The computation starts right behind the incident shock with the “constant specific volume” condition for the duration calculated previously. When the particle encounters

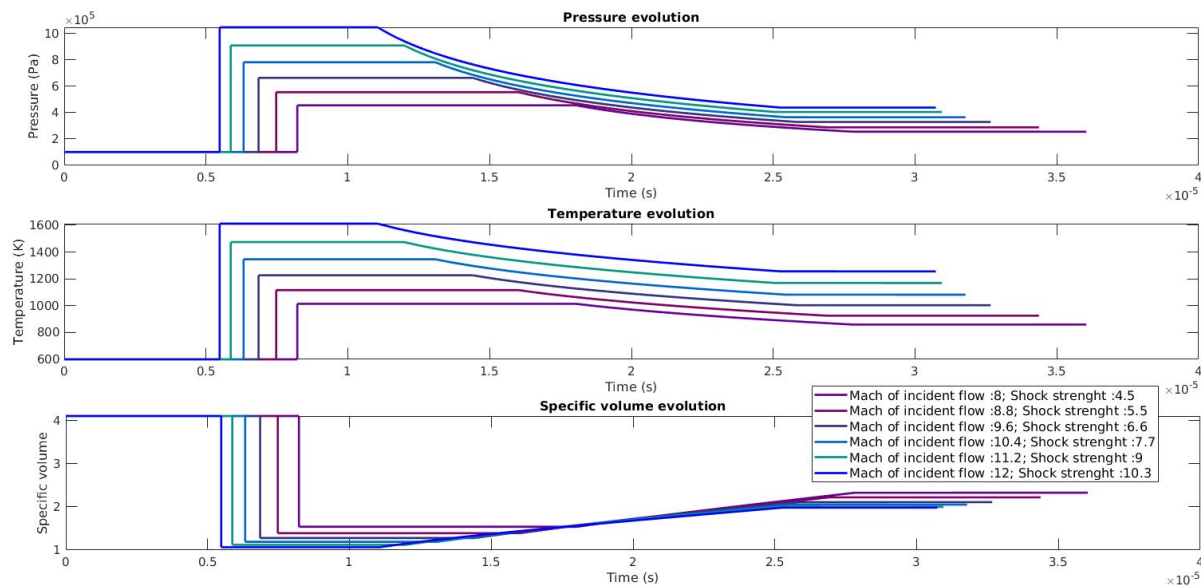


**Figure 2.5:** Regular refraction with reflected Expansion - Evolution of state variables for particle  $x = 10$  cm, at  $\omega_i = 14.5^\circ$ .

the expansion fan, CHEMKIN II is run with the specific volume evolution calculated before. Finally, the condition in zone (3) is again “constant specific volume”. The chemical computation for the particle chosen in figure 2.5 is plotted in figure 2.6. The temperature history allows to detect an ignition characterized by a sharp temperature increase.

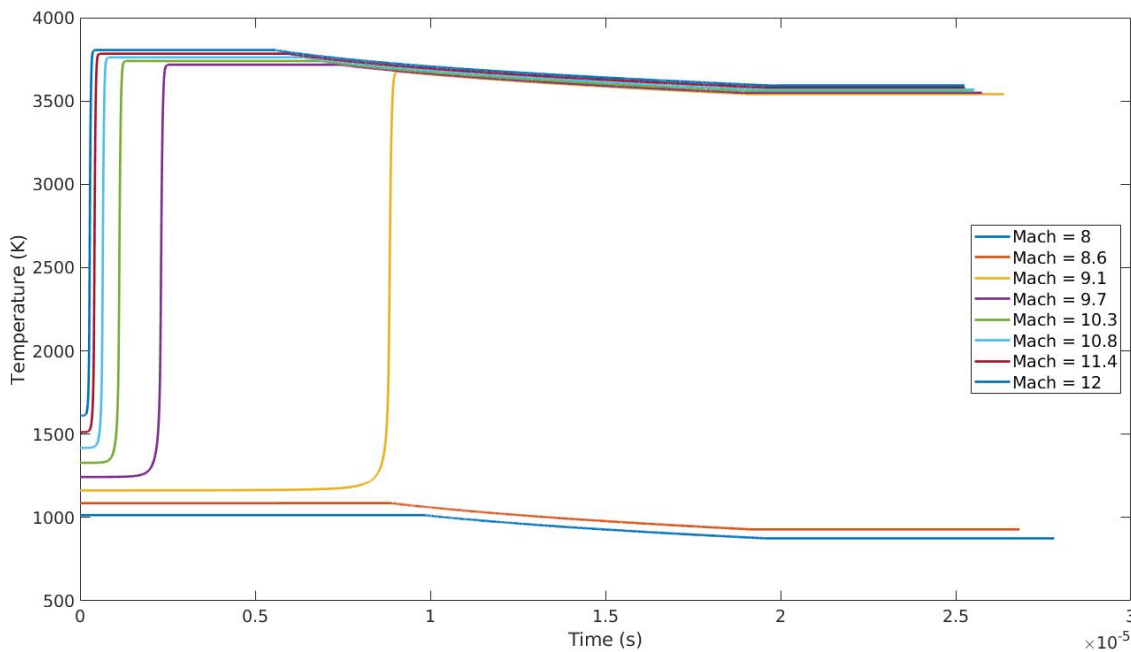


**Figure 2.6:** Regular refraction with reflected Expansion - Chemical simulation for particle  $x = 10$  cm, at  $\omega_i = 14.5^\circ$ .

Defining  $M_{\text{ignit}}$  as the lowest free-stream Mach number for which the particle considered in our example ignites, successful ignitions lie in the range  $M_{\text{ignit}} \in [8.79; 9.19]$ . Note that it is

possible to determine  $M_{\text{ignit}}$  with higher precision and for each particle; figure 2.7 shows that this Mach number varies with the position of the particle considered. For a given free-stream Mach number, some particles ignite and some do not.

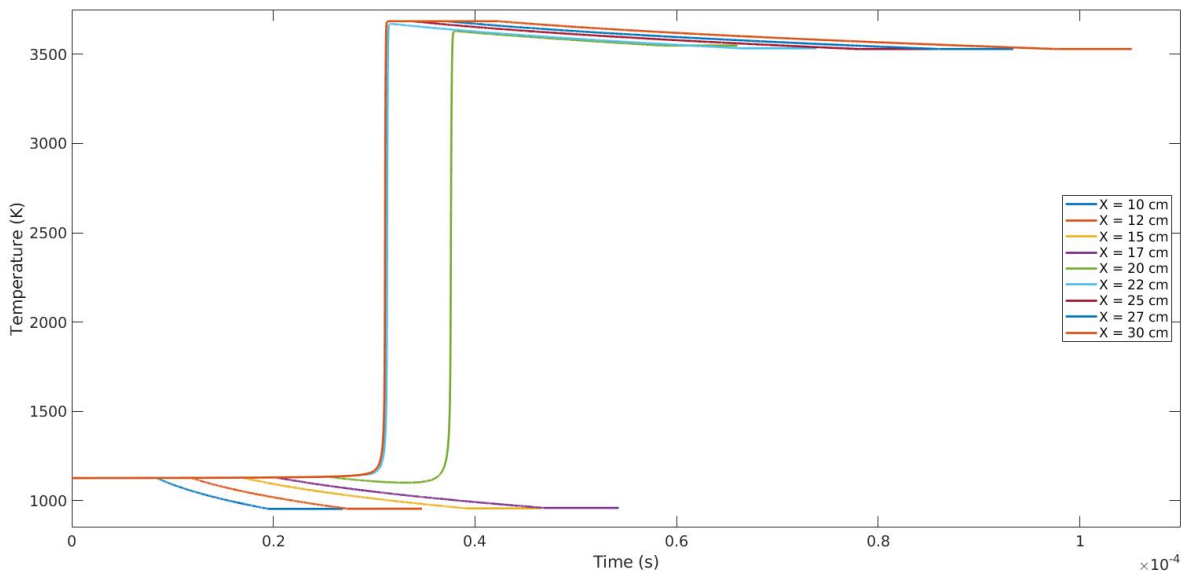


**Figure 2.7: Regular refraction with reflected Expansion** - Chemical simulation for several particles, at  $M_1 = 8.8$ ,  $\omega_i = 14.5^\circ$ .

As a final result, figure 2.8 shows  $M_{\text{ignit}}$  against the position (i.e. abscissa). Since we chose to link abscissa and ordinate of the selected particles, we can note that  $M_{\text{ignit}}$  decreases asymptotically towards  $M_{\text{ignit}} = 8.8$  as we move away from the triple point. However, the free-stream Mach numbers obtained in a spark-ignition engine or in a RCM never reach such values: we concluded that, even if it is theoretically possible, detonation initiation would not occur for a RRE. In fact, it is more likely to occur for irregular refraction structures. More complex phenomena are also involved, such as non planar interfaces, concentration gradients or contaminated gases, which can affect detonation initiation.

## Regular Refraction with Reflected shock

The second regular refraction, RRR, is shown in figure 2.9. Again, this schematic, not drawn to scale, is only a visual tool to understand the evolution along the path of a particle.

As for a RRE pattern, equations A.1 to A.6 allow to go from zone (1) to zone (2) without ambiguity. To go from zone (5) to zone (4), we also used polar diagrams: the intersection of the transmitted shock polar and the reflected shock polar gives  $\xi_t$  and  $\delta_t$ . It is simpler this time to compute zone (3) since it is linked to zone (2) by the shock-jump equations, just as zones (1) and (2) are.

$$P_3 = \xi_r P_2 \text{ and } P_3 = P_4 = \xi_t P_5$$

Knowing  $\xi_t$  allows us to find  $\xi_r$  and to deduce the Mach number in zone (3). Finally, the

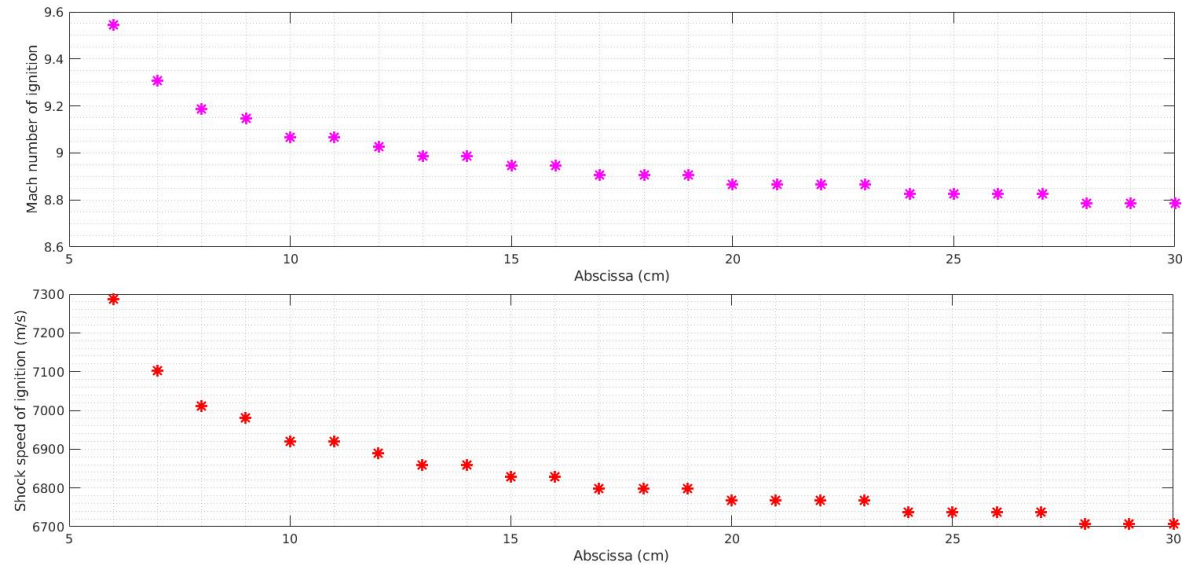


**Figure 2.8:** Regular Refraction with reflected Expansion - Evolution of  $M_{\text{ignit}}$  with the position of the particle.

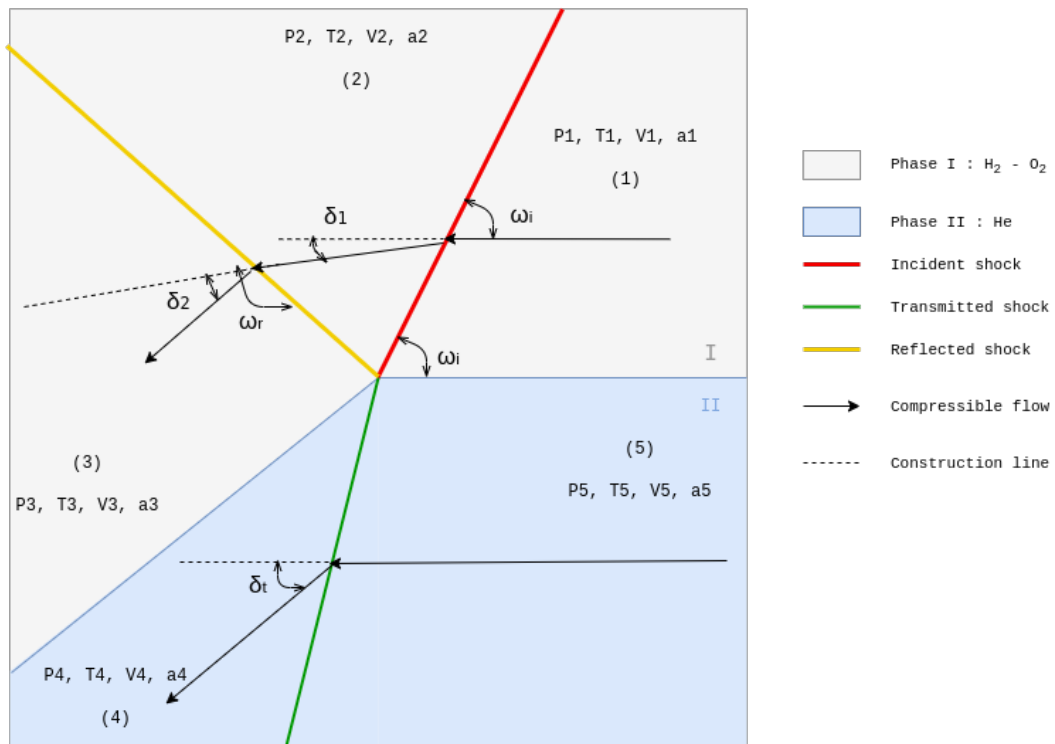


**Figure 2.9:** Notations, zones and angles for *Regular Refraction with Reflected shock pattern*.

conditions in (3) are fully determined using the contact surface relation ( $\delta_t = \delta_1 + \delta_2$ ).

**Gas dynamics results** To run our MATLAB program, we chose  $\omega_i = 21.5^\circ$  as angle of incidence and the strengths of shocks were  $\chi \in [0.6; 1] \iff M_{sh} \in [1; 1.26] \iff M_1 \in [2.76; 3.41]$ .

Figures 2.10 and 2.11 show the evolution of a set of Lagrangian particle for a free-stream Mach number  $M_1 = 3.25$ , see “RRR instance” in figure 2.1. The schematic is now drawn

to scale and the pressure, temperature and specific volume histories allow to observe the influence of the position of the particles.

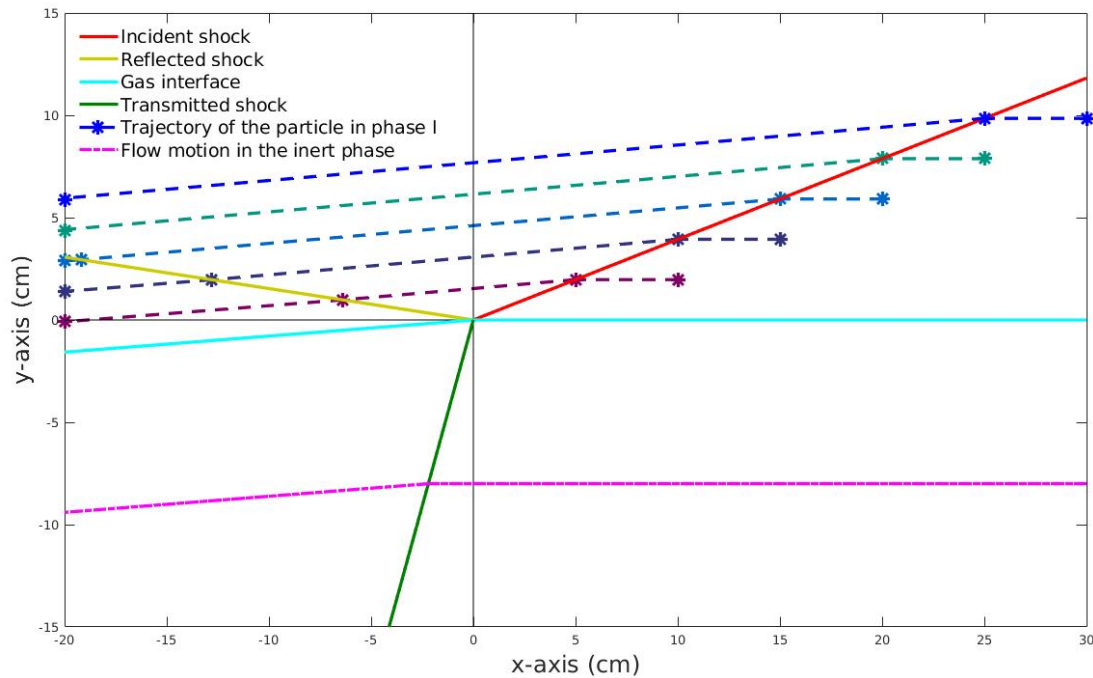


**Figure 2.10:** Regular Refraction with Reflected shock - Schematic of the path of several particles, at  $\chi = 0.67$ ,  $M_1 = 3.25$ ,  $\omega_i = 21.5^\circ$ .

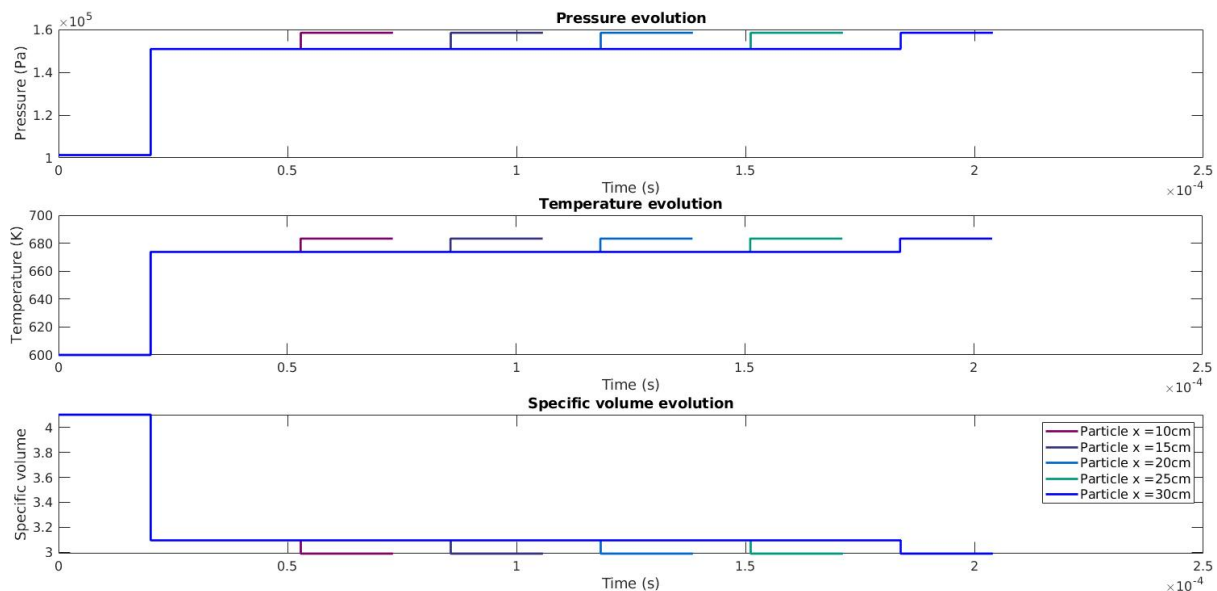


**Figure 2.11:** Regular Refraction with Reflected shock - Evolution of state variables for several particles, at  $\chi = 0.67$ ,  $M_1 = 3.25$ ,  $\omega_i = 21.5^\circ$ .

Figure 2.12 show the influence of the free-stream Mach number for a single particle. The pressure and temperature levels reached are not as high as for RRE pattern. We can expect

that some particles will not ignite because the Mach numbers are not high enough.

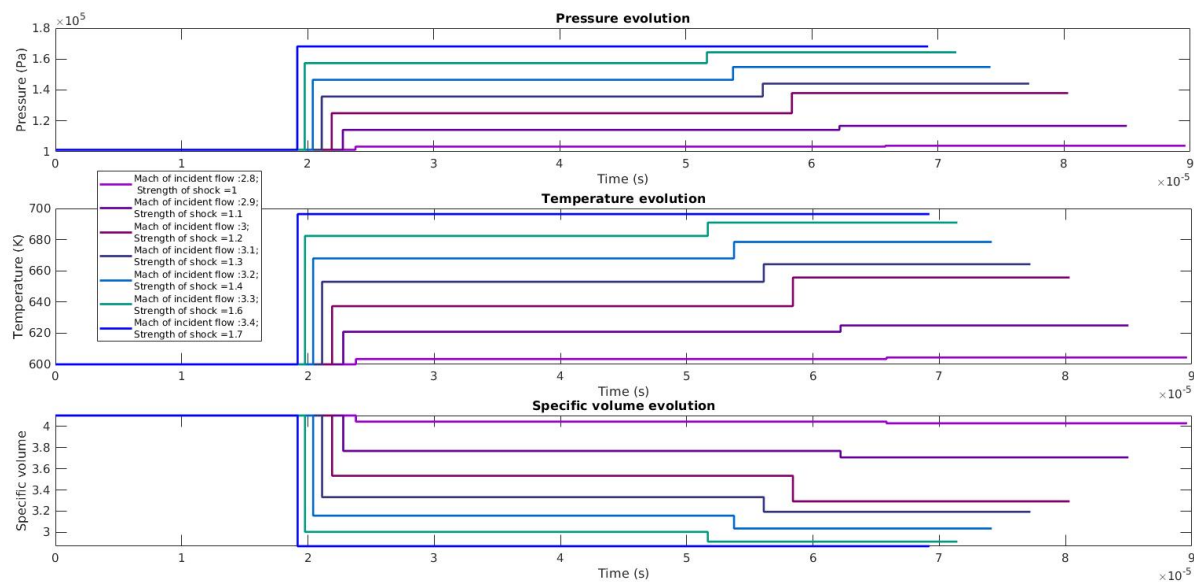


**Figure 2.12: Regular Refraction with Reflected shock - Evolution of state variables for particle  $x = 10$  cm, at  $\omega_i = 21^\circ$ .**

**Reactive results** The CHEMKIN-II simulation starts right behind the incident shock with a “constant specific volume” condition for the duration calculated previously. When the particle encounters the reflected shock, a new simulation is started with initial conditions, i.e. pressure, temperature, specific volume, calculated for zone (3) but with initial composition calculated at the end of zone (2). A “constant specific volume” is considered for this simulation. The reactive simulation for the particle chosen in figure 2.5 is plotted in figure 2.13.

**Non-monotonic evolution of the reflected pressure jump** In figure 2.13, the non-monotonic evolution of the reflected pressure jump  $\xi_r$  with the incident Mach number  $M_1$  is surprising at first. Since polar diagrams are used to determine  $\xi_r$ , it is complex to have a clear overview of the relation between  $M_1$  and  $\xi_r$ . Figure 2.14 provides an unambiguous illustration of the relation between  $M_1$  and  $\xi_r$ . Note that the peak ( $X = 2.947$ ,  $Y = 1.116$ ) is a simulation artefact. The script used to determine the strong solution and the weak solution is based on shock polars which are computed with a finite number of points. For each point of the transmitted polar, the script searches for the nearest point of the reflected polar and calculates the distance between the two. Then, it selects the first pair for which the distance is minimal. Using this simple method allows to accelerate computations. However, in some cases, only the strong solution can be selected because the finite number of points: the weak solution occurs between two calculated points of the reflected shock polar and it cannot be detected. This is what happened in the case of the simulation artefact.

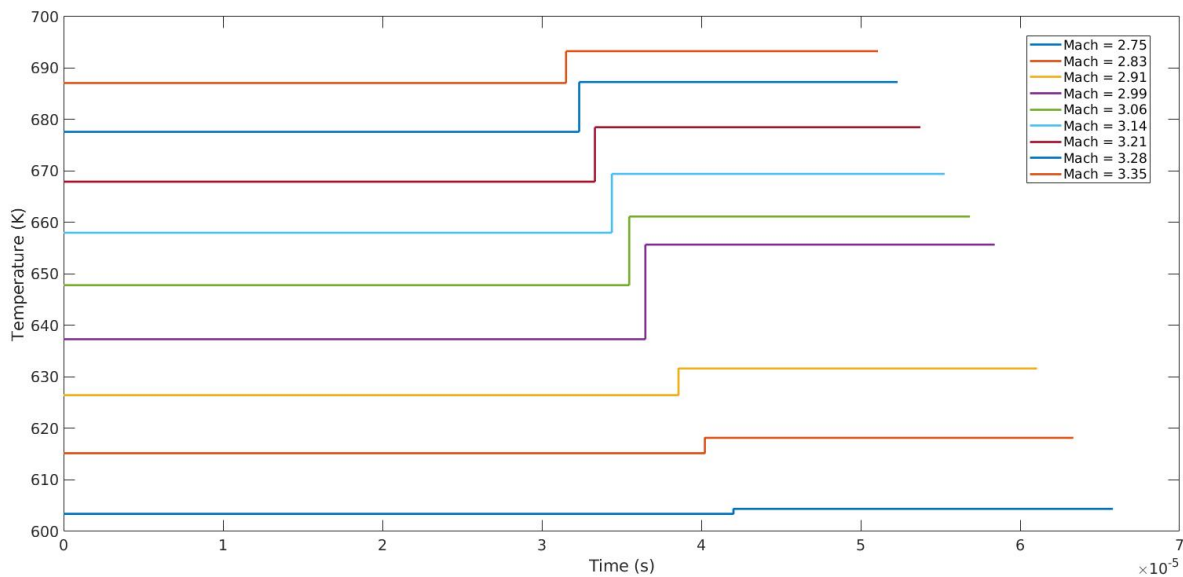


**Figure 2.13:** Regular Refraction with Reflected shock - Chemical simulation for particle  $x = 10$  cm, at  $\omega_i = 21^\circ$ .

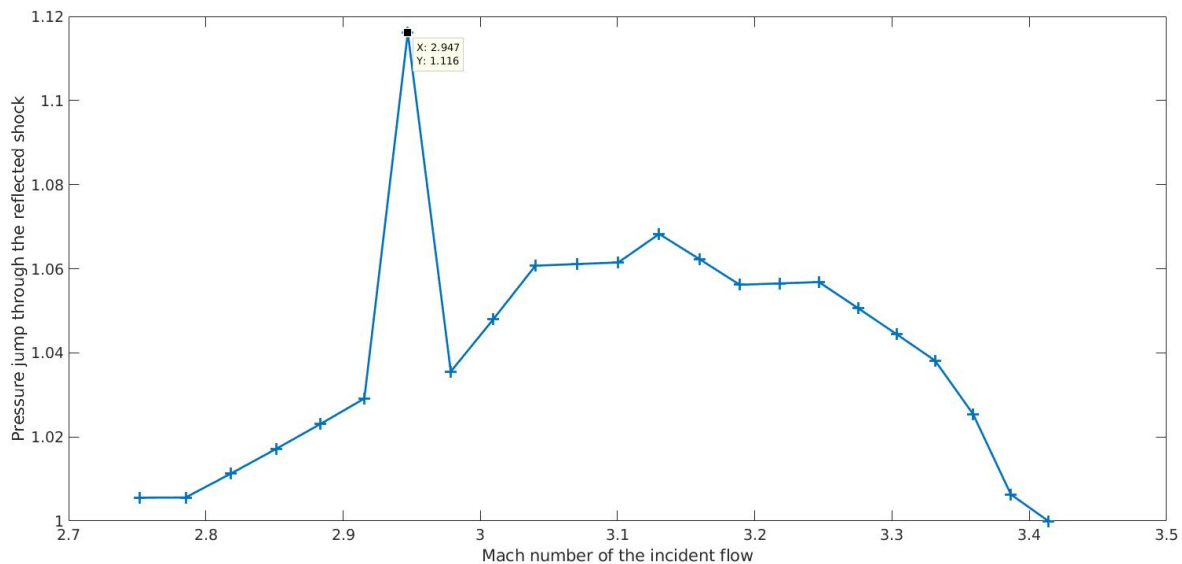


**Figure 2.14:** Regular Refraction with Reflected shock - Evolution of the reflected pressure jump  $\xi_r$  with the free-stream Mach number  $M_1$

Under these conditions, we were not able to detect any significant jump in temperature: the only jump observed is due to the fluid particle passing across the reflected shock, as shown in figure 2.15. We can explain such an observation with the fact that, to obtain a RRR pattern, only weak shocks can occur (see 2.1). With weak shocks, temperature and pressure jumps are not strong enough to induce ignition in the reactive phase.

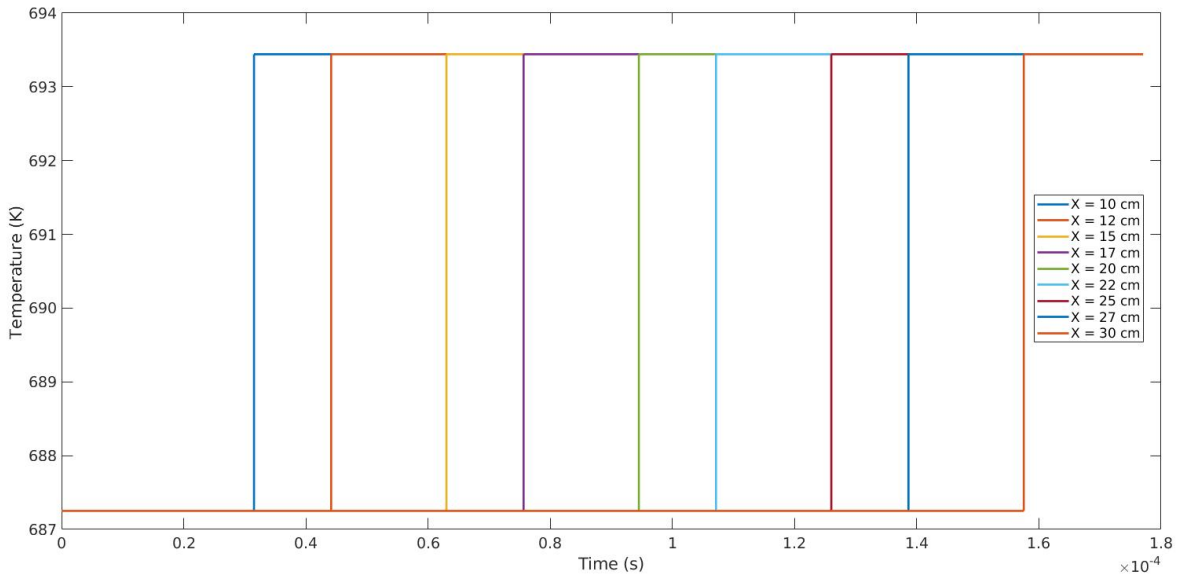


**Figure 2.15: Regular Refraction with Reflected shock - Chemical simulation for several particles, at  $M_1 = 3.4$ ,  $\omega_i = 21.5^\circ$ .**

## 2.4 FAILURE OF THE GENERAL METHOD FOR IRREGULAR PATTERN

As explained in section 1.1, for irregular patterns, it is not possible to use polar diagrams since the reflected wave and transmitted shock polars do not intersect. However, we can use the piston theory developed by [Abd-El-Fattah et al.](#) (see section 1.2).

In the case of a bound precursor, we have another relationship at our disposal [[Abd-El-Fattah et al., 1976](#)]:

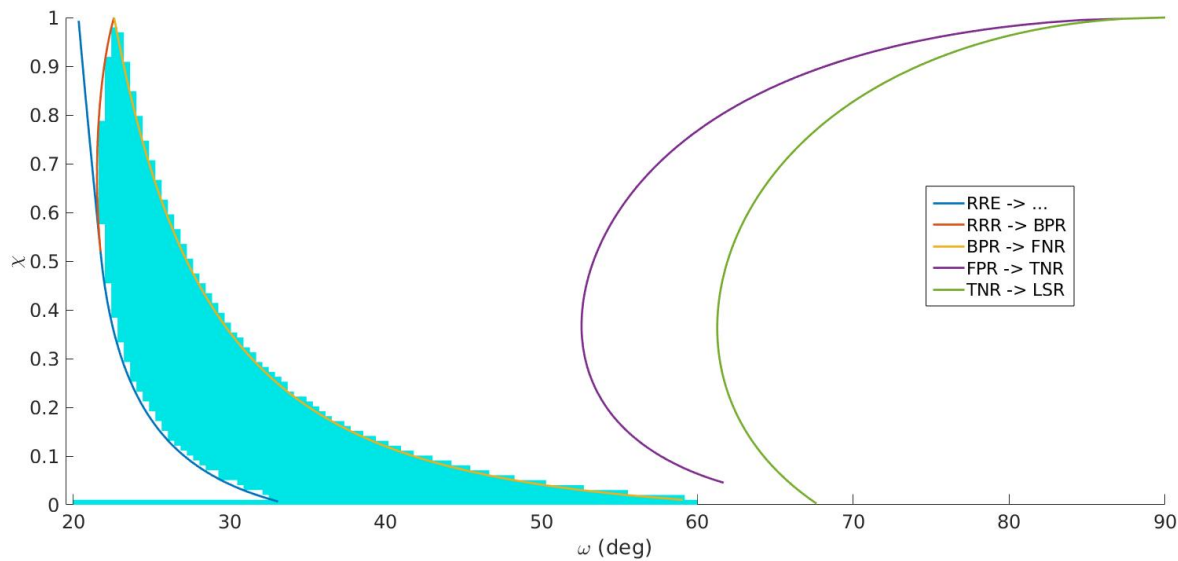
$$\frac{V_i}{\sin \omega_i} = \frac{V_t}{\sin \omega_t} \quad (2.1)$$

where  $\omega_t$  is the angle of incidence of the transmitted shock. The piston theory and equation 2.1 enable to go from zone (5) to zone (4) without ambiguity. Using equations A.1 to A.6 to go from zone (1) to zone (2), we only need to know the nature of the reflected wave.

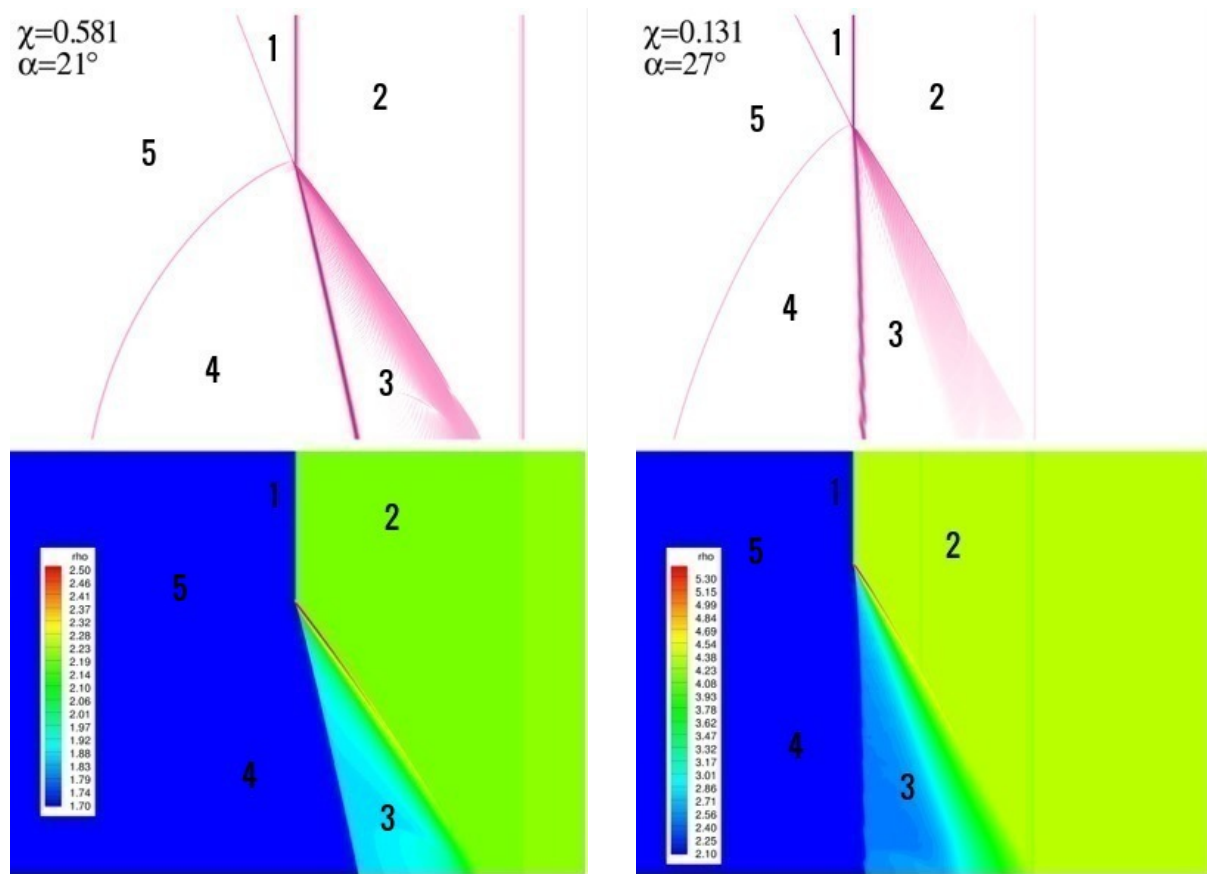
To have a better idea of what can happen in the BPR domain of figure 2.1, we chose to compare the pressures  $P_2$  and  $P_4$  in zones (2) and (4).

Figure 2.16 is a regime diagram for  $H_2\cdot O_2\cdot He$  interface, where the BPR domain has been colored. Regions of the diagram where  $P_2 < P_4$  were supposed to be colored in magenta. However, our computation show that the cyan region covers the entire BPR domain: we may conclude that an expansion occurs in zone (3) for a BPR pattern, whatever are the  $\chi$  and  $\omega_i$  conditions. Such a characteristic was already underlined by [Henderson et al.](#) and [Nourgaliev et al.](#) in the form of a fourth wave. The existence of a fourth wave can also be seen in the simulation made by Stany Gallier in [de Gouvello \[2019\]](#), reproduced here in figure 2.17.

All these observations resulted in the schematic for the BPR pattern shown in figure 2.18



**Figure 2.16:** Regime diagram for  $\text{H}_2\text{-O}_2\text{-He}$  interface. In white, domain where BPR structure does not occur; in cyan, domain of BPR where  $P_2 > P_4$  (reflected expansion); in magenta, domain of BPR where  $P_2 < P_4$  (reflected shock).



**Figure 2.17:** Simulation of a *Bound Precursor Refraction* structure for a Ar-He interface, courtesy of Gallier. Transmitted shock is slightly detached from the refraction point and curved.

with the assumption that our particle is close enough to the refraction point to neglect the curvature of the transmitted shock.

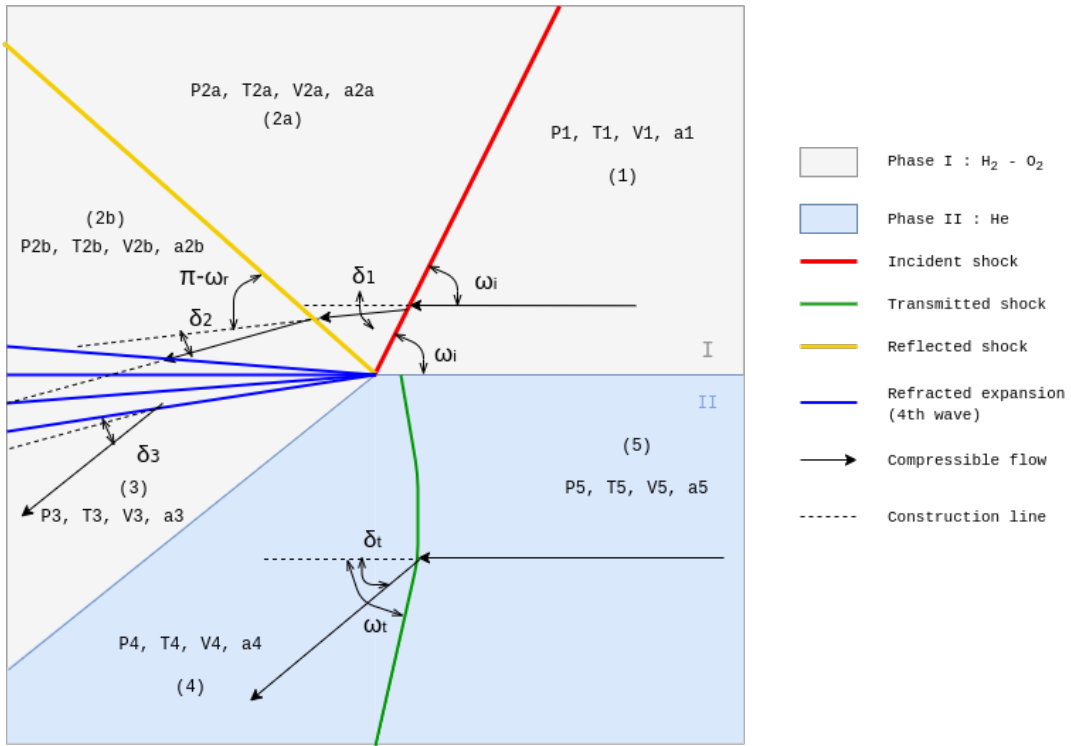


**Figure 2.18:** Notations, zones and angles for *Bound Precursor Refraction* pattern.

However, while computing the state variables in phase I (zones (1), (2a), (2b) and (3)), high discrepancies were obtained across the contact surface. Imposing both pressure equilibrium and equal flow deflection, our computation resulted in a non-physical solution, i.e. pressure jump across reflected shock was less than unity. In other words, the pressure dropped across a shock wave. To confirm our observations, we took figure 2.17 (right) as a reference. We set a Ar-He interface, an incident shock of  $\chi = 0.131$  as inverse strength and  $\alpha = 27^\circ$  as angle of incidence and a reflected shock of approximately  $\omega_r = 177^\circ$  as measured angle of incidence. Starting with a density  $\rho = 1.61$ , our model was able to reproduce the density jump through the incident shock (it predicts  $\rho = 4.36$  behind the incident shock). However, it was unable to reproduce the density jump through the reflected shock (it predicts  $\rho = 8.66$  though the density field does not exceed 5.30 in figure 2.17). We concluded that it was not possible to impose pressure and deflection boundary conditions at the same time for this structure.

The method we used so far is not adequate to reproduce the results computed by Gallier. A potential explanation could be the loss of self-similarity of the structure, as the transmitted shock is detached from the refracted point; additional constitutive relationships or methodologies are thus required. Note that Abd-El-Fattah and Henderson mentioned a loss of self-similarity for LSR structure with a CO<sub>2</sub>-CH<sub>4</sub> interface only. Another explanation is that the curvature of the transmitted shock needs being accounted for, leading to variable flow deflections as we move away from the refraction point, which may explain the discrepancies observed.

# Conclusions

Shock wave refraction at a slow-fast gas-gas interface was studied. A thorough analysis of the relevant literature allowed us to identify all the refraction patterns that have been experimentally realized. Upon critically reviewing regular and irregular structures, together with the previous analysis tools used (i.e. shock polars), the transition boundaries between the patterns were described.

Our numerical results were in overall agreement with the experiments of [Abd-El-Fattah and Henderson](#), except for predicting the FPR-TNR transition. We attributed the inability of our model to predict the latter transition to non-idealities which [Abd-El-Fattah and Henderson](#) took into account, such as the membrane used to keep the gases separate. However, accounting for membrane effects in our computations did not yield appreciable improvements. We are still unable to recover the transition boundary shown in [Abd-El-Fattah et al. \[1976\]](#). We nonetheless deemed our methodology satisfactory and applied it to interfaces in which an inert gas (He) separates a reactive gas ( $H_2 \cdot O_2$ ).

The resulting flow structures (i.e. incident/reflected/transmitted shock angles, expansions, flow deflections, etc.) were used to run chemical kinetics computations in which the thermodynamic changes that arbitrary fluid particles experience as they travel through a regular refraction pattern are included; this allowed us to determine a range of incident Mach numbers for which ignition was likely to occur. For RRE pattern, the critical incident Mach numbers that result in ignition are mostly greater than 8.8. For RRR pattern however, the Mach numbers involved were too low ( $M_1 < 3.4$ ) to result in ignition and potential detonation initiation. Finally, we showed that the methodology employed for regular structures does not seem to be applicable for irregular patterns such as BPR; this is likely due to the assumption of self-similarity made in the formulation of the theory. More sophisticated methods are thus required to analyze the more complex refraction patterns. Future work will include a more thorough analysis using CFD.



# Bibliography

- A.M. Abd-El-Fattah and L.F. Henderson. Shock waves at a slow-fast gas interface. *J. Fluid Mech.*, 89:79–95, 1978. doi: <https://doi.org/10.1017/S0022112078002475>.
- A.M. Abd-El-Fattah, L.F. Henderson, and A. Lozzi. Precursor shock waves at a slow-fast gas interface. *J. Fluid Mech.*, 76:157–176, 1976. doi: <https://doi.org/10.1017/S0022112076003182>.
- J. Anderson. *Fundamentals of Aerodynamics, 6th edition*. Mc Graw Hill Education, 2017.
- G. Ben-Dor. *Shock Wave Reflection Phenomena*. Springer Netherlands, 2007. ISBN 978-3-540-71381-4. URL <https://www.springer.com/gp/book/9783540713814>.
- Y. de Gouvello. Detonation initiation by shock wave refraction. Master's thesis, Tsinghua University and ENSTA Paris, 2019.
- Z. Han and X. Yin. *Shock Dynamics*. Springer Netherlands, 1993. ISBN 978-94-017-2995-6. URL <https://www.springer.com/gp/book/9780792317463>.
- J.-F. Hass and B. Sturtevant. Interaction of weak shock waves with cylindrical and spherical gas inhomogeneities. *J Fluid Mech*, 181:41–76, 1987.
- L.F. Henderson. The refraction of a plane shock wave at a gas interface. *J. Fluid Mech.*, 26: 607–637, 1966. doi: <https://doi.org/10.1017/S0022112066001435>.
- L.F. Henderson. On shock impedance. *J. Fluid Mech*, 40:719–735, 1970. doi: <https://doi.org/10.1017/S002211207000040X>.
- L.F. Henderson. On the refraction of shock waves. *J. Fluid Mech.*, 198:365 – 386, 1989. doi: <https://doi.org/10.1017/S0022112089000170>.
- L.F. Henderson, P. Colella, and E.G. Puckett. On the refraction of shock waves at a slow-fast gas interface. *J. Fluid Mech*, 224:1–27, 1991. doi: <https://doi.org/10.1017/S0022112091001623>.
- R.G. Jahn. The refraction of shock waves at a gaseous interface. *J Fluid Mech*, 1:457–489, 1956.

- Sean McKenna. *Free-surface turbulence and air-water gas exchange*. PhD thesis, MIT, 2014.
- C. Netzer, L. Seidel, M. Pasternak, H. Lehtiniemi, C. Perlman, F. Ravet, and F. Mauss. Three-dimensional computational fluid dynamics engine knock prediction and evaluation based on detailed chemistry and detonation theory. *International Journal of Engine Research*, 19(1):33–44, 2018.
- R.R. Nourgaliev, S.Y. Sushchikh, T.N. Dinh, and T.G. Theofanous. Shock wave refraction patterns at interfaces. *International Journal of Multiphase Flow*, 31:969–995, 2005. doi: 10.1016/j.ijmultiphaseflow.2005.04.001.
- Y. Qi, Z. Wang, J. Wang, and X. He. Effects of thermodynamic conditions on the end gas combustion mode associated with engine knock. *Combustion and Flame*, 62:4119–4128, 2015.
- Y. Wang, S. Xiang, Y. Qi, R. Mével, and Z. Wang. Shock wave and flame front induced detonation in rapid compression machine. *Shock Waves*, 28:1109–1116, 2018.
- Z. Wang, Y. Qi, X.X. He, J. Wang, S. Shuai, and C.K. Law. Analysis of pre-ignition to super-knock: Hotspot-induced deflagration to detonation. *Fuel*, 144:222–227, 2015.
- Z. Wang, Y. Qi, H. Liu, P. Zhang, X. He, and J. Wang. Shock wave reflection induced detonation (swrid) under high pressure and temperature condition in closed cylinder. *Shock Waves*, 26:687–691, 2016.
- Z. Wang, F. Li, and Y. Wang. A generalized kinetic model with variable octane number for engine knock prediction. *Fuel*, 188:489–499, 2017a.
- Z. Wang, H. Liu, and R. Reitz. Knocking combustion in spark-ignition engines. *Progress in Energy and Combustion Science*, 61:78–112, 2017b.
- S. Zeng and K. Takayama. On the refraction of shock wave over a slow-fast gas interface. *Acta Astronautica*, 38:829–838, 1996. doi: [https://doi.org/10.1016/S0094-5765\(96\)00096-3](https://doi.org/10.1016/S0094-5765(96)00096-3).
- W. Zhang, L. Zou, X. Zheng, and B. Wang. Numerical study on the interaction of a weak shock wave with an elliptic gas cylinder. *Shock Waves*, 29:273–284, 2019.

# A. Shock wave and Prandtl-Meyer relationship in gas dynamics

This appendix is inspired from [Anderson \[2017\]](#): some notations can change because they are supposed to match the notations of the present report.

## A.1 CHANGE OF FRAME OF REFERENCE

In the experiments led by [Abd-El-Fattah et al., Abd-El-Fattah and Henderson, Jahn](#), a shock wave is propagating at a certain speed  $u_i$  normal to it in the frame of reference of the laboratory. The flow is assumed to be motionless. However, it is more convenient to study the refraction patterns in the frame of reference of the shock, so as to only take the speed of the flow magnitude into account. The change of frame of reference is illustrated in figure A.1. Figure A.1 also defines the free-stream Mach number of the incident flow  $M_1$  and the Mach number of the incident shock  $M_{sh}$ .

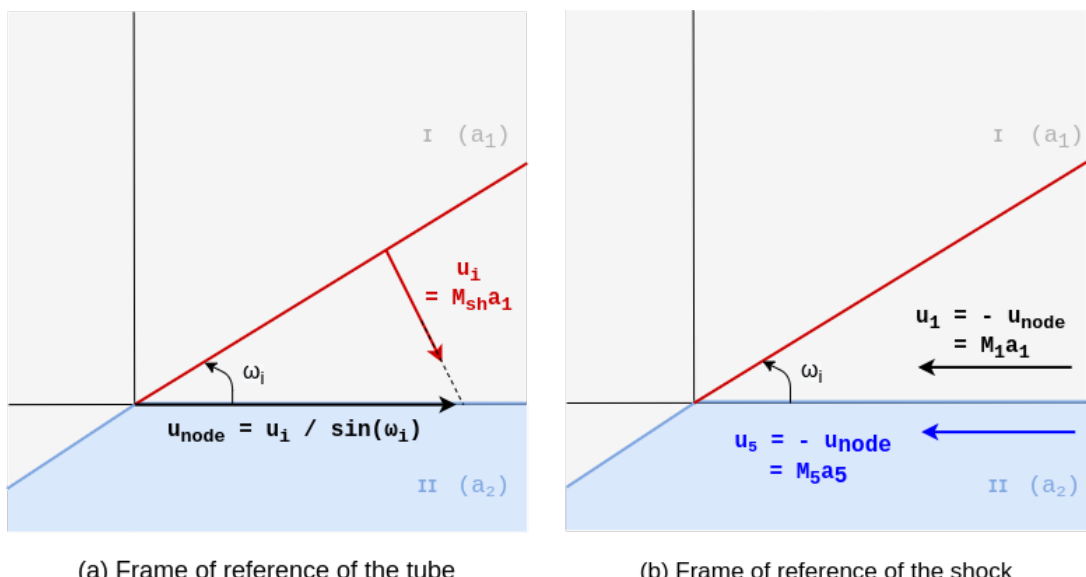


**Figure A.1:** Change of frame of reference: **incident shock, gas interface.**

## A.2 SHOCK-JUMP EQUATIONS

The shock is now motionless and the incident flow travels through it with a non-zero velocity  $u_1$ . For the following equations and in figure A.2, the subscript 1 refers to upstream flow, subscript 2 to downstream flow, **n** to components of vectors which are normal to the shock and **t** to tangential components. The shock propagates in a gas of specific heat ratio  $\gamma$ .

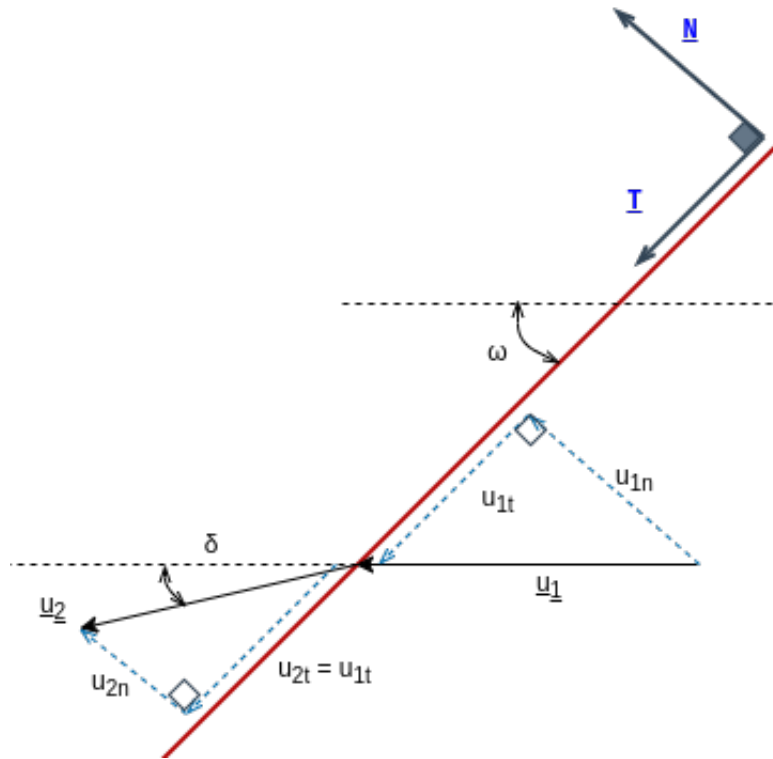


**Figure A.2:** Geometry associated to the oblique shock

Mach number of the incident flow is defined by:  $M_1 = \frac{u_1}{a_1}$ . Knowing  $M_1$  and the angle of incidence of the shock  $\omega$ , it is now possible to calculate the pressure jump  $P_2/P_1$  which is also called strength of the shock and noted  $\xi$ , temperature jump  $T_2/T_1$  and specific volume jump  $V_2/V_1 = \rho_1/\rho_2$ .

To simplify the following formulae, let us define the normal Mach number  $M_{1n} = \frac{u_{1n}}{a_1} = \frac{u_1 \sin(\omega)}{a_1} = M_1 \sin(\omega)$ .

The shock relationship are:

$$\xi = \frac{P_2}{P_1} = \frac{1 - \gamma + 2\gamma M_{1n}}{\gamma + 1} \quad (\text{A.1})$$

$$\frac{V_2}{V_1} = \frac{(\gamma + 1)M_{1n}^2}{2 + (\gamma - 1)M_{1n}^2} \quad (\text{A.2})$$

$$\frac{T_2}{T_1} = \frac{P_2}{P_1} \frac{V_2}{V_1} \quad (\text{A.3})$$

$$M_{2n}^2 = \frac{1 + \frac{\gamma-1}{2} M_{1n}^2}{\gamma M_{1n}^2 - \frac{\gamma-1}{2}} \quad (\text{A.4})$$

$$M_2 = \frac{M_{2n}}{\sin(\omega - \delta)} \quad (\text{A.5})$$

where  $\delta$  is the angle of deflection behind the incident shock.

$$\tan(\delta) = 2 \cot(\omega) \frac{M_{1n}^2 - 1}{M_1^2(\gamma + \cos 2\omega) + 2} \quad (\text{A.6})$$

### A.3 PRANDTL-MEYER EQUATIONS

Expansion waves do not obey the same laws as shock waves because they are not discontinuity surfaces: in some cases, a reflected expansion can be observed in refraction structure, that is why we need the Prandtl-Meyer relationship.

The particularity of Prandtl-Meyer expansion is that the evolution of the flow is isentropic: stagnation properties remain unchanged [Anderson, 2017] and thus the following relationship can be written.

$$\frac{T_2}{T_1} = \frac{1 + \frac{\gamma-1}{2} M_1^2}{1 + \frac{\gamma-1}{2} M_2^2} \quad (\text{A.7})$$

$$\frac{P_2}{P_1} = \left( \frac{T_2}{T_1} \right)^{\frac{\gamma}{\gamma-1}} \quad (\text{A.8})$$

$$\frac{V_2}{V_1} = \frac{P_1}{P_2} \frac{T_2}{T_1} \quad (\text{A.9})$$

$$\delta = \nu(M_2) - \nu(M_1) \quad (\text{A.10})$$

where  $\nu(\cdot)$  is the Prandtl-Meyer function, defined by

$$\nu(M) = \sqrt{\frac{\gamma+1}{\gamma-1}} \arctan \sqrt{\frac{\gamma-1}{\gamma+1} (M^2 - 1)} - \arctan \sqrt{(M^2 - 1)} \quad (\text{A.11})$$



## B. Transition criteria in the regime diagram $(\chi - \omega)$

In the present section, transition criteria from one refraction pattern to another refraction pattern are detailed. Extracts from [Abd-El-Fattah and Henderson \[1978\]](#) are reproduced in italic font and principles of computation are written in normal font.

### B.1 RRE TO RRR OR BPR BOUNDARY

**Extract:** *Theory suggests that the transition RRE -> RRR takes place when  $i$  maps into the intersection point  $A_1$ , between the two primary polars; we denote the coincidence by  $i = A_1$ , and physically it corresponds to the shock impedances of the two gases becoming equal (Henderson 1970). The data supports the theoretical prediction of transition. See figure B.1.*

**Principle of computation:** for each  $\chi \in [0; 1]$ , determine by dichotomy the highest  $\omega_i$  for which the transmitted shock polar intersects the reflected expansion polar. If there is no intersection point between the two shock polars, it means that the reflected wave is a shock (RRR, see figure 1.4) or that the refraction pattern is irregular (BPR, see figure 1.6 (b)).

### B.2 RRR TO BPR BOUNDARY

**Extract:** *A tangency condition forms between the reflected  $r$  shock polar and the primary  $t$  polar, so that  $\alpha_{1,2}$  form a double root, and for still larger  $\omega_0$  both solutions cease to exist. See figure B.2.*

**Principle of computation:** for each  $\chi \in [0.42; 1]$ , determine by dichotomy the highest  $\omega_i$  for which the transmitted shock polar intersects the reflected shock polar. If there is no intersection point between the two shock polars, it means that the refraction pattern is irregular (BPR, see figure 1.6).  $\chi = 0.42$  is the value for which this boundary intersects the RRE to RRR or BPR boundary on the CO<sub>2</sub>-CH<sub>4</sub> regime diagram. For lower values of  $\chi$ , the RRR to BPR boundary has no physical sense.

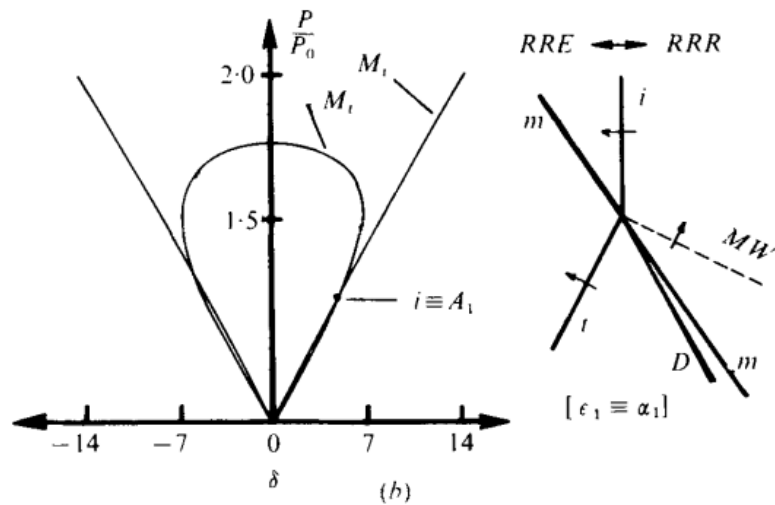


**Figure B.1:** Regular Refraction with reflected Expansion to Regular Refraction with Reflected shock transition (polar diagram - schematic).

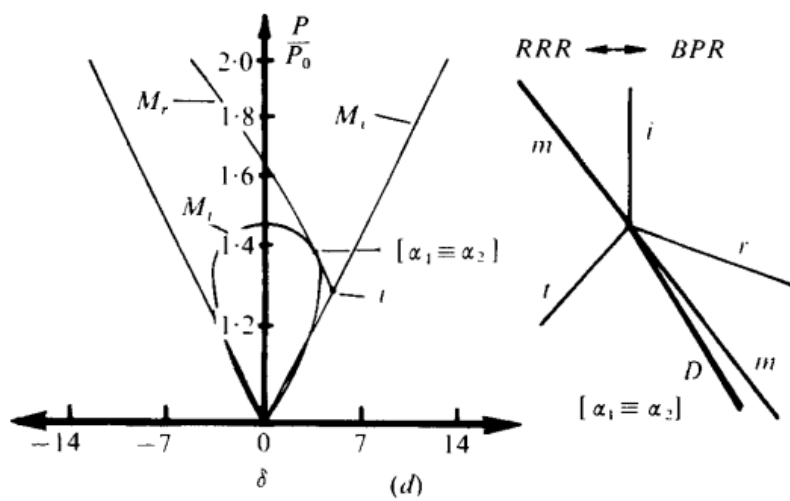


**Figure B.2:** Regular Refraction with Reflected shock to Bound Precursor Refraction transition (polar diagram - schematic).

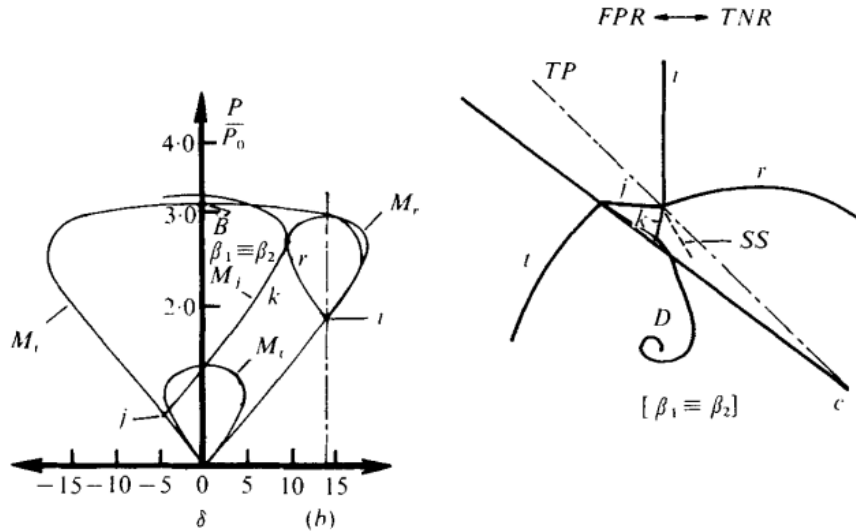


**Figure B.3:** Free Precursor Refraction to Twin von Neumann Refraction transition (polar diagram - schematic).

### B.3 BPR TO FNR BOUNDARY

**Extract:** The transition BPR  $\rightarrow$  FNR can be calculated with the help of Snell's law, for since  $V_{i,t}$  are the velocities of  $i$  and  $t$  normal to themselves, and since  $i$  and  $t$  move along the interface at the same velocity  $V$  in BPR,

$$V = \frac{V_i}{\sin \omega_0} = \frac{V_t}{\sin \omega_t} \quad (1)$$

But at transition  $\omega_t = 90^\circ$ , and therefore its critical angle  $\omega_0 = \omega_F$  can be found from (1) as  $\omega_F = \sin^{-1}(V_i/V_t)$

**Principle of computation:** for each  $\chi \in [0; 1]$ , determine the only  $\omega_i$  which is solution of  $\omega_i = \arcsin(V_i/V_t)$ . The ratio  $V_i/V_t$  is determined thanks to the piston theory explained in section 1.2.

### B.4 FPR TO TNR BOUNDARY

**Extract:** The piston theory is accurate enough to predict the transition FPR  $\rightarrow$  TNR. It will be noted that  $\beta_1$  becomes unreal at or near this condition, which suggests that the condition is determined by the double root (tangency)  $\beta_1 = \beta_2$  or by a near coincidence of  $\beta_1$  with a sonic point. **Note:**  $\beta_1$  and  $\beta_2$  are the two intersection points of r shock polar and k shock polar, see B.3.

**Principle of computation:** for each  $\chi \in [0; 1]$ , determine by dichotomy the highest  $\omega_i$  for which an intersection point exist between the  $k$ -shock polar and the  $r$ -shock polar. Note that the incident shock  $i$  and the  $j$ -shock are two distinct points on the same shock polar. The  $r$ -shock polar is plotted thanks to the conditions behind the incident shock, i.e. it starts at

the  $i$  point in figure B.3. The  $k$ -shock polar is plotted thanks to the conditions behind the  $j$ -shock, i.e. it starts at the  $j$  point in figure B.3. The goal of the dichotomy is then to determine the lowest  $\omega_i$  for which the  $k$ -shock polar and the  $r$ -shock polar do not intersect each other anymore.

## B.5 TNR TO LSR BOUNDARY

**Extract:** *The transition TNR -> LSR occurs at  $M_1 = 1$ .* **Note:** here  $M_1$  is the free-stream Mach number **behind** the incident shock.

**Principle of computation:** for each  $\chi \in [0; 1]$ , determines the lowest  $\omega_i$  for which  $M_2$  the free-stream Mach number **behind** the incident shock becomes subsonic.

## **C. Schedule of the internship**

		Bibliography reading	Getting familiar with code	Transition boundaries	RRE structure	RRR structure	BPR structure
Week 1	05/19						
	05/20						
	05/22						
Week 2	05/25						
	05/26						
	05/27						
	05/28						
	05/29						
Week 3	06/01						
	06/02						
	06/03						
	06/04						
	06/05						
Week 4	06/08						
	06/09						
	06/10						
	06/11						
	06/12						
Week 5	06/15						
	06/16						
	06/17						
	06/18						
	06/19						
Week 6	06/22						
	06/23						
	06/24						
	06/25						
	06/26						
Week 7	06/29						
	06/30						
	07/01						
	07/02						
	07/03						
Week 8	07/06						
	07/07						
	07/08						
	07/09						
	07/10						
Week 9	07/13						
	07/15						
	07/16						
	07/17						
Week 10	07/20						
	07/21						
	07/22						
	07/23						
	07/24						
Week 11	07/27						
	07/28						
	07/29						
	07/30						
	07/31						

**Figure C.1:** Schedule of the internship, from the 18th of May to the 31st of July (11 weeks).